Piezoelectric Soft Robot Inchworm Motion by Tuning Ground Friction Through Robot Shape: Quasi-Static Modeling and Experimental Validation

Zhiwu Zheng, *Member, IEEE*, Prakhar Kumar, Yenan Chen, *Member, IEEE*, Hsin Cheng, *Student Member, IEEE*, Sigurd Wagner, *Fellow, IEEE*, Minjie Chen, *Senior Member, IEEE*, Naveen Verma, *Senior Member, IEEE*, and James C. Sturm, *Life Fellow, IEEE*

***Abstract*—Electrically-driven soft robots based on piezoelectric actuators may enable compact form factors and maneuverability in complex environments. In most prior work, piezoelectric actuators are used to control a single degree of freedom. In this work, the coordinated activation of five independent piezoelectric actuators, attached to a common metal foil, is used to implement inchworm-inspired crawling motion in a robot that is less than 0.5 mm thick. The motion is based on the control of its friction to the ground through the robot's shape, in which one end of the robot (depending on its shape) is anchored to the ground by static friction, while the rest of its body expands or contracts. A complete analytical model of the robot shape, which includes gravity, and contact is developed to quantify the robot shape, friction, and displacement. After validation of the model by experiments, the robot's five actuators are collectively sequenced for inchworm-like forward and backward motion.**

***Index Terms*—Biologically-inspired robots, control, modeling, learning for soft robots, piezoelectrics, soft robot materials and design.**

NOMENCLATURE

Symbol and Definition

q	Distributed mass of the robot per unit length.
R	Bending radius of a single actuator.
κ	Bending curvature of a single actuator.
z_i	Position of the centerline w.r.t. the neutral axis for the ith layer.
I_i	Second moment of area of the i-th layer w.r.t. its centerline.
ϵ_1	Magnitude of the electric field in the PZT layer.
EI	Effective flexural rigidity of the trimorph structure.
γ	Bending curvature per unit voltage of the trimorph structure.
L_{FLAT}	Length of the flat part of the clamped single actuator.
L_{SUS}	Length of the suspended part of a single actuator setup.
$y_{\text{piezo}}(x), y_{\text{weight}}(x)$	Displacement caused by piezoelectric effects and gravity.
$y_{\text{sum}}(x)$	Displacement summing up all the effects (piezoelectricity, gravity, and contact force against the ground.)
$y_{\text{no\_ground}}(x)$	Displacement if there is no contact force.
$y_{\text{ground}}(x)$	Displacement due to contact force.
$F_{\text{shear, ground}}(x)$	Shear force due to contact force.
$f_{\text{ground}}(x)$	Distributed contact force.
$\kappa(x)$	$\gamma V(x)$ $V(x)$ is the voltage applied to each actuator.
$\theta(x)$	$\int_0^x \kappa(x')dx'$.
$y_{\text{piezo}}(x)$	$\int_0^x \theta(x')dx'$.
$F_{g,1}$	Discrete contact force on the lift-off point of Actuator #1.
$F_{g,2B}$	Discrete contact force on the lift-off point of Actuator #2 in Fig. 16(a).
$F_{g,4B}$	Discrete contact force on the lift-off point of Actuator #4 in Fig. 16(a).
$F_{g,2C}$	Discrete contact force on the lift-off point of Actuator #2 in Fig. 16(b).
$F_{g,4C}$	Discrete contact force on the lift-off point of Actuator #4 in Fig. 16(b).
ΔF_{Ground}	Difference of the contact force between the left and the right parts of the robot.
$L_{\text{SUS,LEFT}}, L_{\text{SUS,MID}}$	Lengths of suspended part of Actuator #1 and the middle three actuators.
S_L, S_t	Length and thickness scaling factor of the robot.

Manuscript received 13 January 2023; revised 14 June 2023 and 23 September 2023; accepted 13 November 2023. Date of publication 11 January 2024; date of current version 1 April 2024. This paper was recommended for publication by Associate Editor H. Zhao and Editor A. Menciassi upon evaluation of the reviewers' comments. This work was supported in part by the Semiconductor Research Corporation (SRC), in part by the DARPA, in part by the Princeton Program in Plasma Science and Technology, and in part by the Princeton University. *(Corresponding author: James C. Sturm.)*

The authors are with the Department of Electrical and Computer Engineering, Princeton University, Princeton, NJ 08544 USA (e-mail: zhwzheng.1994@gmail.com; prakhark@princeton.edu; yenanc@zju.edu.cn; hsin@princeton.edu; wagner@princeton.edu; minjie@princeton.edu; nverma@princeton.edu; sturm@princeton.edu).

This article has supplementary downloadable material available at https://doi.org/10.1109/TRO.2024.3353035, provided by the authors.

Digital Object Identifier 10.1109/TRO.2024.3353035

I. INTRODUCTION

WHILE most soft robots are driven by pneumatic power [1], soft robots driven by piezoelectric actuators may be easier to integrate [2], [3], less bulky, faster to respond (with driving frequencies up to thousands of Hertz [4], [5]), lighter, and potentially microsized [6].

Robotic inchworms are appealing because they, in principle, can fit through narrow openings, have no rotating parts, and can be made (in our case) by layering different layers on top of one another. By an inchworm, we mean a robot with a motion cycle (Fig. 1) that involves first raising its midsection while holding its front end fixed on a surface, causing its back end to move forward. In the second step, it releases its front end and fixes its rear end to the surface and extends its body, causing its front end to move forward.

A number of approaches have been explored to achieve such inchworm-like controllable friction and movement. The driving methods include pneumatic actuators [1], [2], [8], [9], heat-induced shape changes [10], [11], embedded magnet pairs controlled by external magnetic field [12], [13], [14], [15], and light-powered liquid crystal elastomer [16]. The inchworm-like bio-inspired motion mechanisms include employing friction films on both ends [9], [17], [18], [19], [20], air suckers at both ends [11], asymmetric and continuous shape change [16], anisotropic friction pads [21], [22], passive or electroactive adhesives [23], [24], [25], sharp hooks [26], and asymmetric feet [10], [13], [27].

In this article, we describe a new mechanism to enable inchworm motion by holding one end of such an inchworm robot fixed, and using its shape alone to change the profile of its contact force on the ground, and hence, control its friction profile. This mechanism is validated by analytical models and experiments. Further, while our work uses only the shift in the contact force profile to cause one end to be fixed while the other moves, the ability to control the contact force on one end versus the other will clearly be important for other inchworm types, which use some kind of "friction pad" on one end or the other.

Our soft-robot design comprises five piezoelectric actuators on a single substrate. The central three actuators cause the central section to lift off the ground and contract or expand laterally. This article shows that the contact force of the robot on the ground can be shifted between the two ends by lifting the head or tail off the ground using the 1st or the 5th actuator. Lifting one end raises the contact force against the ground next to it, and reduces the contact force at the farther end. The robot/ground interface, thus, will have more friction at the lifted end and less friction (enabling it to slide) at the opposite end, as the maximum static friction force is proportional to the contact force against the ground. The effect is analogous to an inchworm's ability to choose which end has "sticky feet" (Fig. 1).

The main contribution of this article is to demonstrate both analytically and experimentally that this "friction asymmetry" between the two ends of a 2-D piezoelectric soft robot can be electrically controlled by lifting one of the far ends off the ground (using a piezoelectric actuator), enabling a tunable "inchworm-type motion." In support of this, the rest of this article is organized as follows.

1) Section II introduces the robot design and structure.
2) In Section III, we develop an analytical model of the robot's shape, including the effects of gravity, on how much of the flexible body lifts off the ground, as a function of the voltages applied to the piezoelectric actuators. The model is compared with experiments, using a robot built from commercially available piezoelectric actuators [28].
3) In Section IV, we analytically derive the difference in the contact force against the ground on one end versus the other end as a function of piezoelectric voltages and provide experimental validation.
4) In Section V, making use of the resulting asymmetry in friction between the two ends, we experimentally demonstrate forward and reverse motion of the robot and compare it with the model.
5) Further, in Section VI, to enable the extrapolation of the results presented here to other experimental conditions, we show how the results would scale to similar robots of different lengths and thicknesses. Finally, Section VII concludes this article.

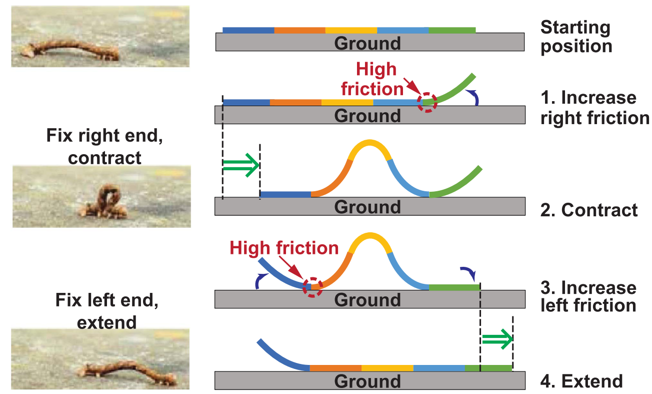

Fig. 1. Inchworm motion [7] and analogous robot motion of "contract" and "extend" cycles in four steps. The robot consists of five thin-film piezoelectric actuators (each shown in a different color) on a common substrate. Raising the actuator on one end increases the friction on that end relative to the opposite end, enabling crawling motion.

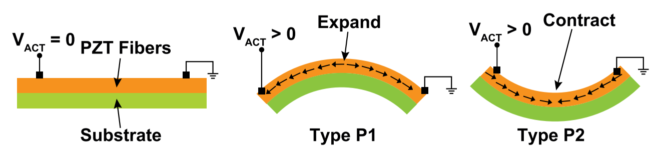

Fig. 2. Mechanism of bending. Type P1 PZT devices bend concave down with positive applied voltage and type P2 devices bend concave up. [29].

II. Robot Design and Construction

Each actuator of Fig. 1 is realized with a 300-μm-thick thin-film lead-zirconate-titanate (PZT) device bonded with 100 μm of epoxy to a thin (50-μm) steel substrate. Applying a positive voltage causes the piezoelectric material to expand or contract laterally, resulting in the assembly curling down or up. (Fig. 2). We used commercially available piezoelectric fiber composite devices [29].

Five piezo devices were laminated onto a single steel foil (50 cm long, 2.5 cm wide) to create the robot (Fig. 3). The PZT actuators we used are recommended for use with only one sign of applied voltage, since they degrade if the opposite sign of voltage

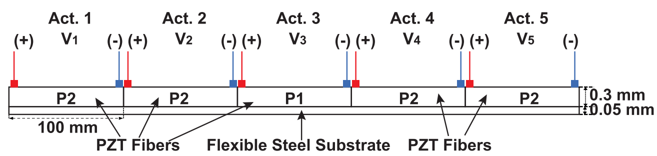

Fig. 3. Cross section of a five-actuator soft robot prototype, 500 mm long and 25 mm wide. Each actuator includes a piezoelectric device made of a PZT fiber composite, controlled by voltage signals wired from off-robot voltage supplies. All PZT devices are attached to a common 50-μm-thick steel foil substrate.

is applied. Because our high-voltage supplies we used had only a positive output, in our experiments, we used two kinds of commercially-available piezoelectric composite actuators: One optimized for curling down (when on top of a flexible substrate) with a positive applied voltage (Type P1) as in Fig. 2, and the second optimized for curling up with a positive applied voltage (Type P2), with voltage polarity defined by the markings on each actuator. Thus, Type P2 actuators (numbers 1, 2, 4, and 5 in Fig. 3) only curled up, and Type P1 actuators (number 3 in Fig. 3) only curled down.

However, for a more general model, the analyses in this article of the robot shape due to piezoelectric effects assume all actuators have the properties of Type P2, with negative voltages used to cause the central actuator (#3) to curl down. The magnitude of the free strain per volt of the Type P1 actuators used in actuator #3 is a factor of 1.7 smaller than that of the Type P2 actuators (0.75 versus 1.3 ppm/V). Thus, the experimental applied voltages used on actuator #3 in our work are -1.7 times those in the modeling.

Fig. 4(a) shows the top view of the robot, and Fig. 4(b) shows the side view while it is actuated. Thin gold wires are connected from the solder pads on the actuators to high-voltage supplies. The system is put in a Faraday cage and contains the robot prototype as well as power and control electronics [Fig. 4(c)].

III. Soft Body Robot Model: Shape

Realizing inchworm action relies on alternately raising the friction of the robot against the ground, between the left and right ends of the robot. Predicting and controlling this friction requires knowledge of the exact shape of the robot including the effects of gravity on the shape. What is also critical is the profile of the vertical force between the actuator and the ground (which we refer to as "contact force" distribution).

This section develops an analytical static model of the robot and contact force distribution as a function of applied voltages on the actuators.

A. Previous Work

Control of the robot requires precise analytical modeling. Current methods of modeling a piezoelectric soft robot have typically employed constant-curvature models [30], [31], [32] and pseudorigid body models [20], [33], [34], [35]. A constant-curvature model treats an actuator (or part of it) as a perfect arc with some radius. Then, a coordinate transformation can be used to model the kinematics of the robot, a procedure similar to that used for a rigid robot. Alternatively, a pseudorigid body model breaks a flexible robot into short rigid links connected by flexible joints. One can further include the effects of gravity by applying Cosserat rod theory to a continuum robot in a cantilever case [36].

In this article, we develop an analytical soft-body model for our robot, which includes gravity and the robot's interaction with the ground. Though previously under-investigated, gravity effects are significant and of critical importance because of the robot's elasticity.

B. Soft Robot Shape Modeling

1) Summary of the Model: When voltages are applied to the actuators, some parts of the robot are flat on the ground, and other parts lift off. In this section, we develop a model that predicts the shape considering piezoelectricity and gravity. The key property of the model is a self-consistent approach to determining which part of the robot lifts off the ground.

We developed the model following a "bottom-up" approach in three steps:

1) a single actuator clamped on one end;
2) three actuators bending to compress in length like an inchworm; and
3) a five-actuator inchworm robot, as in Fig. 1.

Our modeling is based on the Euler–Bernoulli small-amplitude model of displacement y versus the lateral position x. In such a model, for an actuator with a single applied voltage, the shape is determined by the following physical effects:

i) Piezoelectric effect: $d^2y/dx^2 = \gamma V$, where V is the applied voltage, and γ is a constant related to material properties with a unit of $\mathrm{m}^{-1} \cdot \mathrm{V}^{-1}$. See Appendix A2 for details.
ii) Distributed load q (mass per length): $d^4y/dx^4 = \frac{qg}{EI}$, where EI is the effective flexural rigidity of our three-layer (trimorph) structure (Appendix A2).
iii) Discrete external vertical force F: $d^3y/dx^3 = F/EI$.
iv) Discrete load mass m: discontinuity in $d^3y/dx^3 = -mg/EI$ (g is the gravitational constant).

The model must be applied piecewise because the actuator voltage changes from one section to another, and because in some sections the actuator is lying on the ground, whereby the ground applies a vertical force on the actuator.

The following boundary conditions are applied to the solutions:

i) dy/dx must always be continuous, including at all interfaces between different actuators.
ii) Defining the flat ground as $y = 0$, y must be ≥ 0 (easily extended in more complex arrangements).
iii) The ground must support the weight of the actuator—represented by a "contact force" $F_{\text{Ground}}(x)$ acting on the robot, as described later.
iv) The total torque on an unconstrained robot about its center of mass must be zero.

This model assumes a small vertical deformation of the robot, such that the bending amount must be much less than its length.

We now apply this model to increasingly complex shapes, which underlie the motion of our soft robot. We first analyze a single-actuator cantilever (with one end clamped and the other

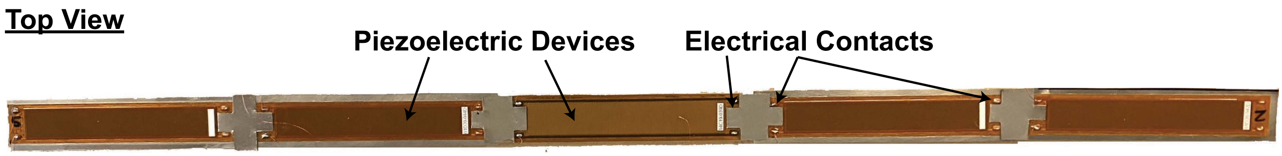

(a)

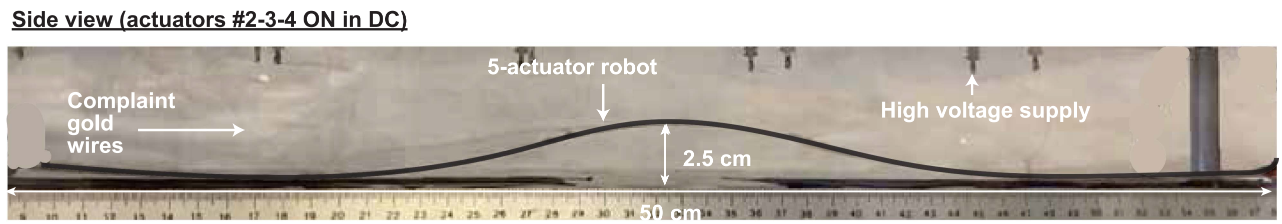

(b)

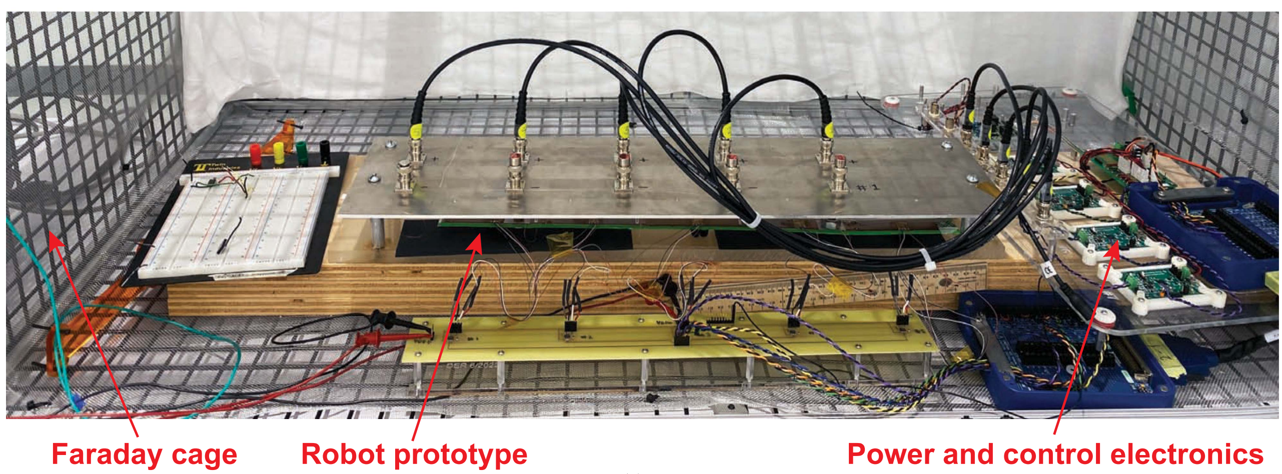

(c)

Fig. 4. Robot setup: (a) Top view. (b) Side view when the central three actuators are turned ON. The five-actuator robot is sitting on a rigid acrylic base, wired to high-voltage supplies with thin gold wires. [20] (c) System setup: The system is in a Faraday cage and contains the robot prototype and the power and control electronics.

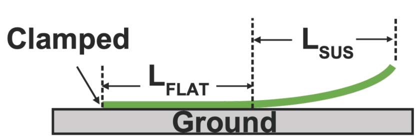

Fig. 5. One-actuator setup on the ground with the left end clamped. A negative voltage is applied to make the actuator bend up. One part of it (L_{FLAT}) lies flat on the ground due to gravity, and the other part (L_{SUS}) is suspended in the air.

end free) on the ground, and then, proceed to the more complex cases.

2) Single Actuator With One End Clamped Parallel to the Ground: Fig. 5 shows one actuator placed on the ground with the left end clamped. When voltage is applied to make the actuator bend up, part of it (L_{FLAT}) stays flat on the ground due to clamping and gravity and the other part (L_{SUS}) lifts up. Our goal is to analytically find the suspended length L_{SUS}.

In the suspended region ($0 \leq x \leq L_{\mathrm{SUS}}$), $x = 0$ is defined at the point that the robot starts to lift off the ground. The shape of a beam clamped on one end with a distributed gravitational load [37] is well known, as well as the quadratic shape of an unloaded (no gravity) piezoelectric actuator clamped at one end [38]. By superposition, the shape of the piezoelectric actuator subjected to gravity and clamped on one end ($x = 0$) is then

$$y(x) = \frac{1}{2}\gamma V x^2 - \frac{qg}{24EI}x^2\left(x^2 - 4L_{\mathrm{SUS}}x + 6L_{\mathrm{SUS}}^2\right). \quad (1)$$

A self-consistent approach (Fig. 6) is proposed to solve L_{SUS}: For small L_{SUS}, we easily see that dy/dx is always ≥ 0, so the suspended region is indeed suspended. For large L_{SUS}, y might become negative at some x, but this is not consistent with our assumption of the actuator being off the ground. Thus, for any applied voltage, only a finite length lifts off the ground. The region to the left of the suspended ("lift-off") section has $y = 0$ and $dy/dx = 0$.

Because we assume the slope is zero on the left end of the actuator, we examine the second derivative at the left end to determine L_{SUS}. Fig. 7 shows the second derivative components caused by piezoelectricity, gravity, and their sum. Since the piezoelectricity contribution to d^2y/dx^2, defined as $d^2y_{\mathrm{piezo}}/dx^2$, is constant and the gravity contribution

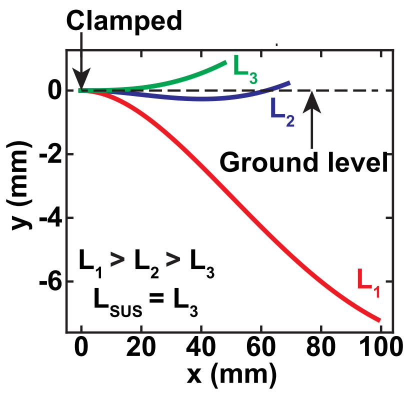

Fig. 6. Plot of shape for an actuator curling up, with the left end clamped at $y = 0$ and $dy/dx = 0$. The suspended length L_{SUS} would be the largest L (L_3) that makes the result physical, i.e., all $y(x) > 0$.

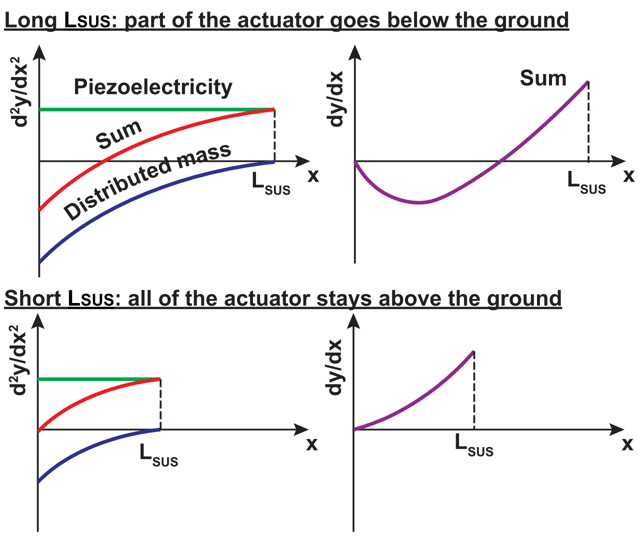

Fig. 7. Second and first derivatives of the shape caused by piezoelectricity, gravity, and their sum for different suspended lengths.

$d^2y_{\mathrm{weight}}/dx^2$ is monotonically increasing, when a "trial" lift-off length L_{SUS} is too long, the second derivative of the sum d^2y/dx^2 is negative at $x = 0$. So dy/dx becomes negative when $x > 0$. Since $y|_{x=0} = 0$, y goes negative as well. This result is not physical, as we assumed $y > 0$ everywhere due to the ground level.

When reducing the lift-off length, d^2y/dx^2 increases. When $d^2y/dx^2|_{x=0}$ reaches 0, dy/dx becomes positive when $x > 0$, and the actuator is always above ground. This means that L_{SUS} is the solution of $d^2y/dx^2|_{x=0} = 0$. Taking the second derivative of (1) and setting it equal to 0 at $x = 0$ ($x = 0$ is the point that the actuator starts to lift off), one finds

$$L_{\mathrm{SUS}} = \sqrt{\frac{2EI}{qg}\gamma V}. \tag{2}$$

Substituting for L_{SUS} from (2) into (1), we have $y(x)$ analytically. For the suspended portion:

$$y(x) = -\frac{qg}{24EI}x^4 + \frac{\sqrt{2}}{6}\sqrt{\frac{qg}{EI}\gamma V}x^3 \tag{3}$$

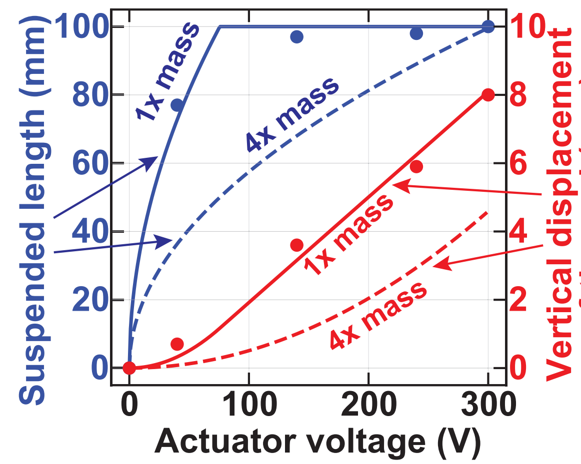

Fig. 8. Suspended length L_{SUS} (blue) and displacement (red) of the free end, versus the driving voltage for a single actuator with one end clamped parallel to the ground. Model (solid lines) and experimental measurements (points) show close agreement. Dashed lines represent the modeling when mass is increased by a factor of four.

while for the flat portion, we have $y(x) = 0$.

We should note that the suspended length L_{SUS} cannot exceed the actuator length L. We need to limit L_{SUS} at L, if the result from (2) exceeds L. In this case, instead of (3), (1) becomes

$$y(x) = \frac{1}{2}\gamma V x^2 - \frac{qg}{24EI}x^2\left(x^2 - 4Lx + 6L^2\right). \tag{4}$$

Fig. 8 plots L_{SUS} and displacement at the lifted end versus actuator voltage, predicted from the model and measured from experiments. The parameter values are listed in Appendix A1. Model and experiments show good agreement without any fitting parameters. Moreover, we recently began experiments to add onboard batteries, control, and high-voltage circuitry [3], [39], [40]. This can easily increase the mass of the robot by a factor of four. Assuming the mass is uniformly distributed, we used the above approach to find the effect of the extra mass. The results (dashed lines in Fig. 8) show such a mass is expected to reduce the vertical displacement by a factor of ~2. This illustrates the importance of including gravity in the models.

3) Five-Actuator Robot—The Middle Three Actuators: Next, we consider how the model predicts the shape of the middle three actuators (Actuators #2–#4) when placed on the ground and curling up in a symmetric fashion ($V_2 = V_4 \geq 0$, $V_3 \leq 0$). Fig. 9 shows a schematic cross-section of the assembly in flat (top) and in bending (bottom) conditions. The left and right ends remain on the ground. We define the lateral length of the total suspended section as L_{SUS}.

In this central suspended section, where there is no force on the robot from the ground, combining piezoelectricity with the Euler–Bernoulli beam equation, defining $x = 0$ at the middle of Actuator # 3, one finds

$$y(x) = -\frac{1}{24}\frac{qg}{EI}x^4 + \frac{1}{2}a_2x^2 + y_{\mathrm{piezo}}(x) + a_0 \tag{5}$$

where $y_{\mathrm{piezo}}(x)$ is a function (defined below), which results from piezoelectricity. In the region of actuator #3 ($-L/2 < x <$

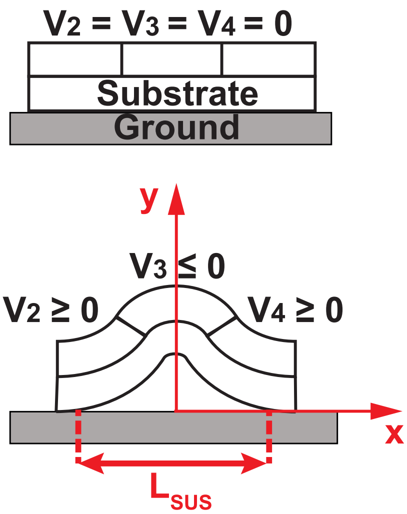

Fig. 9. Three-actuator assembly with voltages applied such that the center bends concave down and the wings concave up. The projected length of the curved assembly is shorter than its flat length. The central portion of length L_{SUS} is suspended.

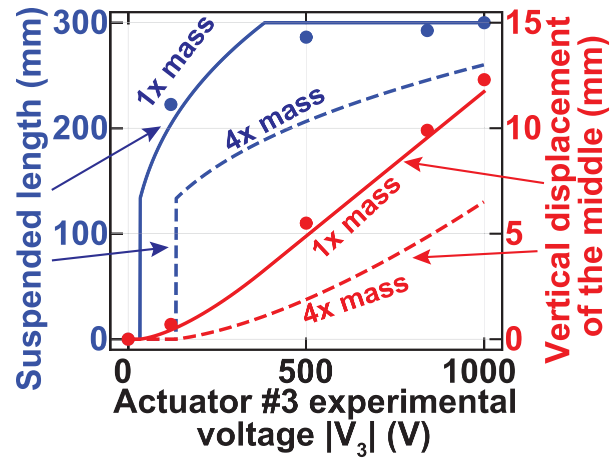

Fig. 10. Suspended length L_{SUS} (blue) and the elevation of the center (red) versus the experimental positive voltage applied to actuator #3 for the three-actuator system, where experimental voltages $V_2 = V_4 = 0.3V_3$. Model (lines) and experimental measurements (points) match well. (The model voltages for the Actuator #3 are -0.58 times the experimental voltages used in the x-axis.) As in Fig. 8, the effect of increasing the robot mass by four times is also shown.

$L/2$), where the piezo effect bends the structure concave down

$$y_{\text{piezo}}(x) = -\frac{1}{2}\gamma|V_3|x^2, \left(-\frac{L}{2} \leq x \leq \frac{L}{2}\right). \tag{6}$$

In the regions of Actuators #2 and #4 ($L/2 < |x| < 3\,L/2$)

$$y_{\text{piezo}}(x) = \begin{cases} \frac{1}{2}\gamma|V_4|x^2 - \frac{1}{2}\gamma\left(|V_3| + |V_4|\right)L \cdot x \\ +\frac{1}{8}\gamma\left(|V_3| + |V_4|\right)L^2 \\ \left(\frac{L}{2} \leq x \leq \frac{3\,L}{2}\right) \\ \frac{1}{2}\gamma|V_4|x^2 + \frac{1}{2}\gamma\left(|V_3| + |V_4|\right)L \cdot x \\ +\frac{1}{8}\gamma\left(|V_3| + |V_4|\right)L^2 \\ \left(-\frac{3\,L}{2} \leq x \leq -\frac{L}{2}\right). \end{cases} \tag{7}$$

The constants a_0 and a_2 of (5) are obtained from the boundary conditions $y|_{x=L_{\text{SUS}}/2} = 0$ and $dy/dx|_{x=L_{\text{SUS}}/2} = 0$

$$a_0 = \frac{1}{384}\frac{qg}{EI}L_{\text{SUS}}^4 + \frac{1}{4}L_{\text{SUS}}\frac{dy_{\text{piezo}}}{dx}|_{x=\frac{L_{\text{SUS}}}{2}} - y_{\text{piezo}}|_{x=\frac{L_{\text{SUS}}}{2}}) \tag{8}$$

$$a_2 = \frac{1}{24}\frac{qg}{EI}L_{\text{SUS}}^2 - \frac{2\frac{dy_{\text{piezo}}}{dx}|_{x=\frac{L_{\text{SUS}}}{2}}}{L_{\text{SUS}}} \tag{9}$$

Similar to the analysis in Section III-B2 for a single actuator, L_{SUS} satisfies $d^2y/dx^2|_{x=L_{\text{SUS}}/2} = 0$. Therefore, if $L_{\text{SUS}} \geq L$

$$L_{\text{SUS}} = \sqrt[3]{12\gamma\left(|V_3| + |V_4|\right)L\frac{EI}{qg}}. \tag{10}$$

Because we only have three actuators, L_{SUS} has a maximum of $3\,L$.

By substituting (6)–(9) into (5), one finds

$$y(0) = -\frac{1}{384}\frac{qg}{EI}L_{\text{SUS}}^4 + \frac{1}{8}\gamma\left(|V_3| + |V_4|\right)L(L_{\text{SUS}} - L). \tag{11}$$

Physically, $y(0)$ must be greater or equal to 0 for a valid solution, giving a minimum value for applied voltages to have a central section of the robot off the ground. For our parameters, the minimum voltage is ~30 V for the "1× mass" case.

The actuators' shape is derived by substituting L_{SUS} into (5), combining (6), (7), and (8).

Fig. 10 plots L_{SUS} and displacement at the midpoint predicted from the model and measured from experiments, as a function of V_3, and $V_2 = V_4 = 0.3V_3$. (The voltage ratio comes from the ratio of the maximum recommended voltages for the P2 and P1 actuators. [29]). (The model voltages for the Actuator #3 are -0.58 times the experimental voltages used in the x-axis.) As in the case of a single actuator, model and experiments match well. Increasing mass by a factor of four is expected to reduce the vertical displacement by a factor of two, again illustrating the importance of including gravity in the models.

As the center of the robot lifts off the ground when voltages are applied, so that the two ends should come closer to one another, one might ask if friction could limit the sliding of the two ends toward each other. Consider three attached actuators, suspended except at the extreme ends. The actuators weigh ~3 g each for a total of 10 g, for a frictional force ~0.1 N, assuming a (large) friction coefficient equal to 1. The "blocking force" of our actuators (what is required to prevent piezoelectric contraction or expansion) ranges from 70–150 N (from the datasheets). Thus, as confirmed by experiment, friction should have little effect on the final piezoelectric shape when the suspended height is much less than the suspended length.

4) Five-Actuator Robot: Fig. 11 shows a schematic cross-section sketch of a five-actuator robot, corresponding to the arrangement introduced in Figs. 3 and 4. Actuators #1 to #5 have applied voltages V_1 to V_5. $V_1 \geq 0$, $V_5 \geq 0$, $V_2 = V_4 \geq 0$, and $V_3 \leq 0$.

We first *analytically* examine two cases relevant to robot motion.

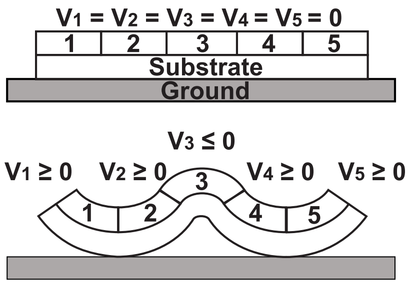

Fig. 11. Five-actuator robot prototype on the ground. Applying voltages to elements 2, 3, and 4 lifts the center, and makes the projected length of the robot shrink.

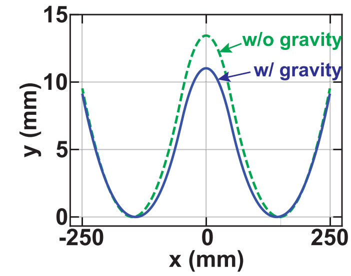

Fig. 12. Numerical solution of the model for robot shape when $V_1 = 300$ V, $V_2 = 300$ V, $V_3 = -580$ V (corresponding to 1000 V in the experiment), $V_4 = 300$ V, and $V_5 = 300$ V with and without gravity. With gravity, the single points that touch the ground are at $x = -141.9$ mm and $x = 141.9$ mm. Without gravity, they are -148.1 mm and 148.1 mm.

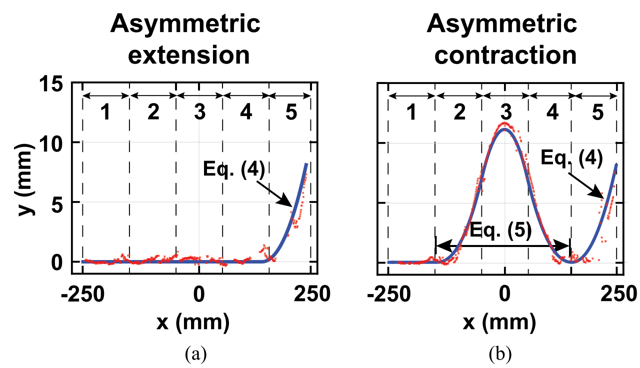

Fig. 13. Robot shapes: Five-actuator model versus experiment. (a) Act #5 is turned ON (numbers 1–5 identify the location of the five actuators); (b) Act #2–#5 are turned ON for two steps in a movement cycle (Steps 1 and 2 of Fig. 1). (Steps 3 and 4 are symmetric to these two). Voltages when ON: $V_1 = 300$ V, $V_2 = 300$ V, $V_3 = -580$ V in modeling (+1000 V in experiment with Type P1 actuator), $V_4 = 300$ V, and $V_5 = 300$ V. Blue lines are modeling result, and red points are points measured from a cross-sectional image of the robot.

1) When the voltages applied are low, the interfaces between Actuators #1 and #2, and #4 and #5 have a flat section, so that we separate the analysis of the robot into three parts: Section III-B2 above applies to Actuator #1 and #5, and Section III-B3 applies to Actuators #2, #3, and #4.
2) When the voltages applied are high enough, the flat regions near the interfaces of Actuators #1 and #2, and #4 and #5, shrink to zero length, so that the robot touches the ground at only two single points. Separate sections of the robot cannot be analyzed independently as described just above, and we need to find where these points are, which we define as x_L and x_R. $x = 0$ is defined as the middle point of the robot. The equation for the shape of the robot depends on location with respect to this x_L and x_R

$$y(x) = \begin{cases} y_L(x) & -\frac{5}{2}L < x \le x_L \\ y_M(x) & x_L < x \le x_R \\ y_R(x) & x_R < x \le \frac{5}{2}L \end{cases} \tag{12}$$

These three shapes all are described by the same form (a fourth-order polynomial), but the coefficients of the terms depend on the applied voltages in each section and the relevant boundary conditions.

$$\begin{pmatrix} y_L(x) \\ y_M(x) \\ y_R(x) \end{pmatrix} = \begin{pmatrix} a_{01} \\ a_{02} \\ a_{03} \end{pmatrix} + \begin{pmatrix} a_{11} \\ a_{12} \\ a_{13} \end{pmatrix} x + \frac{1}{2} \begin{pmatrix} a_{21} \\ a_{22} \\ a_{23} \end{pmatrix} x^2 + \frac{1}{6} \begin{pmatrix} a_{31} \\ a_{32} \\ a_{33} \end{pmatrix} x^3 - \frac{1}{24} \frac{qg}{EI} x^4 + y_{\text{piezo}}(x). \tag{13}$$

The twelve parameters a_{ij}, x_L, and x_R depend on the applied voltages. They can be found numerically by using the following fourteen boundary conditions: $y_L(x_L) = y_M(x_L) = 0$; $y'_L(x_L) = y'_M(x_L) = 0$; $y''_L(x_L) = y''_M(x_L)$;$y_M(x_R) = y_R(x_R) = 0$; $y'_M(x_R) = y'_R(x_R) = 0$; $y''_M(x_R) = y''_R(x_R)$; $y''(-5/2L) = y''_{\text{piezo}}(-\frac{5}{2}L)$, $y'''(-5/2L) = 0$; $y''(5/2L) = y''_{\text{piezo}}(5/2L)$, $y'''(5/2L) = 0$.

Fig. 12 shows the numerically calculated solution for $V_1 = 300$ V, $V_2 = 300$ V, $V_3 = -580$ V (which would correspond to 1000 V in the experiment), $V_4 = 300$ V, and $V_5 = 300$ V with and without gravity. Note that with gravity, the ground contact points are not at the actuator junctions themselves but only slightly ($\sim$8 mm) inside the actuators' junctions 1/2 and 3/4.

If smaller actuator voltages are applied, a "flat spot" inside and possibly including the actuator 1/2 and 3/4 interfaces will result, and the lift-off points of the central section will be inside the 1/2 and 3/4 interfaces. Then, one can exactly calculate the shape of the suspended hump of the central section, including gravity effects, using (5)–(10).

5) Five-Actuator Robot. Comparison Between Model and Experiment: We now compare the model solution to experimental measurements for the four steps of the inchworm motion cycle shown schematically in Fig. 1.

The applied voltages for actuators when ON are $V_1 = 300$ V, $V_2 = 300$ V, $V_3 = -580$ V in modeling (+1000 V in experiment with Type P1 actuator), $V_4 = 300$ V, and $V_5 = 300$ V, (Recall, because actuator #3 has a different sign and magnitude of piezoelectric coefficient than actuators #1, #2, #4, and #5, its applied voltage when ON was of the opposite sign and larger than that of the other actuators, as discussed earlier in Section II).

Fig. 13 shows modeled and experimental robot shapes during two of the four sequential steps in an inchworm movement cycle as described in Fig. 1 (with the other two steps being symmetric to these). The voltages are the same as in the previous section. The shape predicted from this model matches closely with experiments. As we describe later, having one end actuator in the air and the other flat leads to asymmetry in friction between the left and right ends of the robot, which is a key to its lateral motion.

We note three omissions in our model, relative to the actual robot design. First, in the actual robot, only ∼85% of the length of each actuator is "active" piezoelectric, with the remaining length required for electrical contacts and packaging. Second, while the substrate width is 2.5 cm, the piezoelectric width is only 2.0 cm, which reduces the expected curvature by 8%, based on straightforward mechanical modeling. Given the inevitable uncertainties in the many other experimental parameters, we ignored these effects.

Third, our 2-D model inherently ignores torsional distortion, i.e., twisting, which could in principle occur when the robot width is narrow and a long central section is suspended off the ground. In experiments with a robot width of 2 cm with a maximum suspended length of 30 cm and a height of 2.5 cm [e.g., cross-sectional images, such as Fig. 4(b)], any twisting caused a change in the height of one edge of the robot of less a minimum observable amount of ∼1 mm.

6) Lateral Motion Per Inchworm Cycle: The amount of forward (or backward) motion from the four-step cycle in Figs. 1 and 13 is predicted analytically using our model, by assuming the right end remains fixed in Step 2 and the left end remains fixed in Step 4. Since the substrate is a steel foil, with a high Young's modulus, its *total* length does not appreciably change during the robot operation. Therefore, the net lateral movement over one cycle is the difference between its lateral length (projection in the x-direction) from Step 1 to 2, or from Step 3 to 4, which we call $L_{x,\mathrm{contract}}$, where $y(x)$ is given by (5)–(10), as shown in Fig. 9. One finds

$$\begin{aligned} L_{x,\mathrm{contract}} &= L_{\mathrm{tot}} - L_x \\ &= \int_{-3\,L/2}^{3\,L/2} \left(\sqrt{1 + \left(\frac{dy}{dx}\right)^2} - 1 \right) dx \\ &= 2 \int_0^{L_{\mathrm{SUS}}/2} \left(\sqrt{1 + \left(\frac{dy}{dx}\right)^2} - 1 \right) dx. \end{aligned} \tag{14}$$

When $|dy/dx| \ll 1$, this reduces to

$$L_{x,\mathrm{contract}} \approx \int_0^{L_{\mathrm{SUS}}/2} \left(\frac{dy}{dx}\right)^2 dx. \tag{15}$$

This length difference results from the region of Actuators #2, #3, and #4, corresponding to a range in the x-axis from $-3\,L/2$ to $+3\,L/2$ (as defined in Fig. 9).

Furthermore, because $|dy/dx| \ll 1$ even for the maximum piezoelectric voltages, when (10) applies to L_{SUS}, the length contraction $L_{x,\mathrm{contract}}$ is approximated as

$$\begin{aligned} L_{x,\mathrm{contract}} &= (|V_3| + |V_4|)\, \gamma L^3 \sqrt[3]{\left(\frac{qg}{EI}\right) \gamma^2 L^2 \left(|V_3| + |V_4|\right)^2} \\ &+ \frac{33\sqrt[3]{12}}{1120} \left(|V_3| + |V_4|\right)^2 \gamma^2 L^2 \sqrt[3]{\left(\frac{EI}{qg}\right) \gamma L \left(|V_3| + |V_4|\right)} \\ &- \frac{1}{12} \gamma^2 L^3 \left(|V_3| + |V_4|\right)^2 \\ &- \frac{1}{1920} \frac{qg}{EI} \gamma L^5 \left(|V_3| + |V_4|\right). \end{aligned} \tag{16}$$

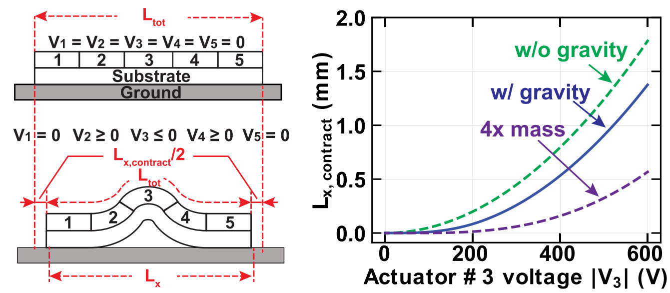

(a) (b)

Fig. 14. (a) Schematic view. (b) Modeled lateral motion per inchworm cycle (contraction of length in the -direction in Actuators #2 to #4) $L_{x,\mathrm{contract}} = L_{\mathrm{tot}} - L_x$ versus the magnitude of actuator #3 voltage $|V_3|$, with $V_2 = V_4 = 0.5|V_3|$, with V_3 as large as -580 V (corresponding to +1000 V in the experiment). With gravity, $L_{x,\mathrm{contract}}$ and, thus, lateral movement per cycle are up to 1.1 mm. The cases with mass increased four times (purple dashed line) and without gravity (green dashed line) are also plotted.

When the middle three actuators are all suspended, since the piezoelectric effect is enough to fight the gravity effect, as was noted earlier in Section III-B3, L_{SUS} will be limited at $3\,L$. In this case, $L_{x,\mathrm{contract}}$ reduces to

$$\begin{aligned} L_{x,\mathrm{contract}} &= \frac{1}{18} \left(|V_3| + |V_4|\right)^2 \gamma^2 L^3 - \frac{(|V_3| + |V_4|)\gamma qg L^5}{12EI} \\ &+ \frac{81 q^2 g^2 L^7}{2240 (EI)^2}. \end{aligned} \tag{17}$$

When the piezoelectricity is weak, $L_{\mathrm{SUS}} = 0$. Therefore, $L_{x,\mathrm{contract}} = 0$.

Fig. 14 shows the lateral motion per cycle $L_{x,\mathrm{contract}}$ as a function of the magnitude of Actuator #3 voltage $|V_3|$ ($V_3 \leq 0$), while $V_2 = V_4 = 0.5|V_3|$ and $V_1 = V_5 = 0$ V. $L_{x,\mathrm{contract}}$ increases monotonically with increasing magnitude of V_3 and reaches 1.3 mm when $V_3 = -600$ V (corresponding to 1000 V in the experiment). For comparison, Fig. 14 also shows the expected contraction per length with no gravity. We see that for our experimental robot, gravity is expected to reduce the motion per cycle by ∼22%. Increasing the mass by a factor of four is expected to further reduce the motion per cycle by a factor of three.

IV. Soft Body Robot Model: Contact Force Against the Ground and Friction Asymmetry

In this section, we use the robot shape to determine the force that the ground exerts on the robot, as a function of location. We then go on to determine the difference in total contact force against the ground (and thus the friction experienced) between the left and right sides of the robot, as a function of the applied actuator voltages.

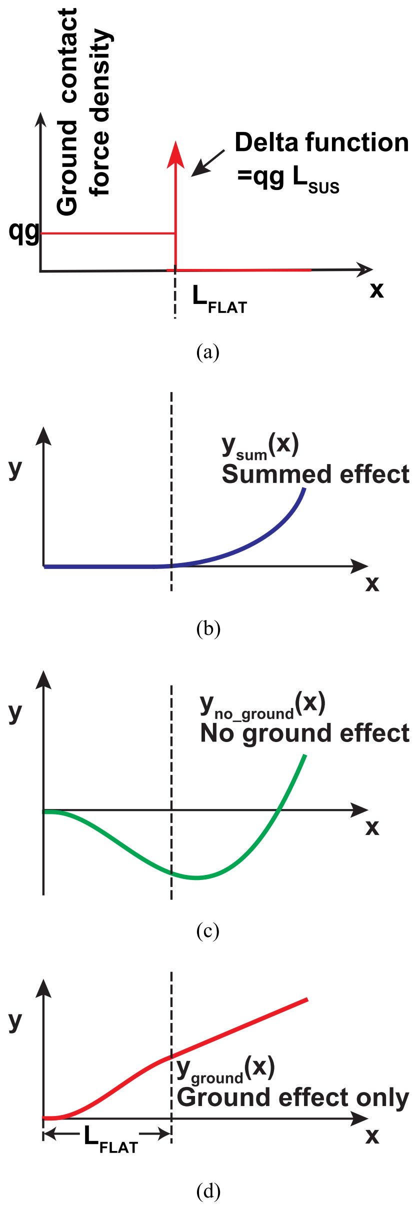

Fig. 15. (a) Ground contact force distribution of a single actuator with its left end clamped on the ground. (b), (c), (d) Actuator shape separating the effect of the contact force.

A. Contact Force Against the Ground for a Single Clamped Actuator

We start with the shape of a single actuator with one end clamped parallel to the ground as derived in Section III-B2, (3). The distribution of the contact force per unit length pushing up on the actuator ("ground contact force density") is then derived by noting that in the Euler–Bernoulli model, the lateral distribution of the total vertical force on the robot (gravity pulling down minus the ground pushing up) is given by the fourth derivative of the shape. Adding the distributed gravitational force $q \cdot g$ (where q is mass/length and g is 9.8 N/kg) then gives the contact force pushing up on the robot.

Fig. 15(a) shows the result (not including the force exerted by the clamp). For the section lying flat on the ground, there is no shear force. For an infinitely small segment, as there is no shear force applied on the left end or the right of this segment, gravity and the contact force against the ground on this segment need to be balanced. Therefore, the distributed contact force against the ground equals the distributed load, which is a constant that equals qg (load per length times gravitational constant). However, for the section lifting off the ground, the contact force is zero, since the robot and the ground are not in contact. For the point where "lift-off" begins, the shear force on the flat (left) side is zero (no bending), but the suspended (right) part has the gravity of the whole suspended part acting on it. Therefore, the contact force on the "lift-off" point would be the gravitational force of the suspended part, and the density is thus a delta function with amplitude equal to the suspended part's gravity.

The contact force distribution can also be understood by separating the gravity and ground-force effects. Fig. 15(b) shows the modeled shape of an actuator ($y(x)$) with applied voltage considering all the physical effects, including piezoelectric, gravity, and contact force effects [repeated from Fig. 6, given by (3)]. Fig. 15(c) shows the shape considering only piezoelectric and gravity force effects (i.e., "No ground effect"), with shape given by

$$y_{\text{no\_ground}}(x) = -\frac{qg}{24EI}x^4 + \frac{qgL}{6EI}x^3 + \left(\frac{1}{2}\kappa - \frac{qgL^2}{4EI}\right)x^2 \tag{18}$$

corresponding to a suspended cantilever. Finally, the difference of these two cases, shown in Fig. 15(d), then represents the contact force only, given by

$$\begin{aligned} y_{\text{ground}}(x) &= y_{\text{sum}}(x) - y_{\text{no\_ground}}(x) \\ &= \frac{qg}{24EI}x^4 - \frac{qgL}{6EI}x^3 + \left(\frac{qgL^2}{4EI} - \frac{1}{2}\kappa\right)x^2. \end{aligned} \tag{19}$$

To the right of the point where the actuator lifts up, there is no force on the actuator, and thus, its shape is a straight line.

The shear force caused by the contact force is proportional to the third derivative of the displacement $y_{\text{ground}}(x)$

$$\begin{aligned} F_{\text{shear, ground}}(x) &= -EI\frac{d^3 y_{\text{ground}}}{dx^3} \\ &= qgL - qgx \qquad (0 \le x \le L_{\text{FLAT}}) \end{aligned} \tag{20}$$

and for the suspended part $(x > L_{\text{FLAT}})$

$$F_{\text{shear, ground}}(x) = 0 \quad (x > L_{\text{FLAT}}). \tag{21}$$

Therefore, the distributed contact force is

$$f_{\text{ground}}(x) = \begin{cases} qg + qgL_{\text{SUS}}\delta(x - L_{\text{FLAT}}) & (0 \le x \le L_{\text{FLAT}}) \\ 0 & (x > L_{\text{FLAT}}). \end{cases} \tag{22}$$

B. Contact Force and Friction Asymmetry for the Robot

1) Theory: Inchworm motion relies on the ability to alternate the "stickiness" between the two ends. In this section, we show how this can be achieved by raising one end of the robot (Actuator #1 or #5) off the ground. This raises the static friction at that end, and lowers it at the other end, resulting in the

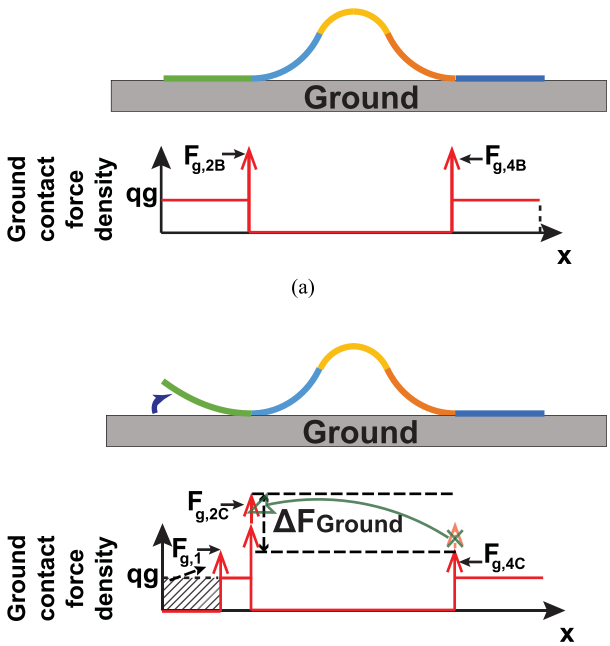

Fig. 16. Mechanism of asymmetry in contact force against the ground (and, therefore, in friction) between the two ends of the robot ("seesaw" effect). (a) Acts #2–#4 are turned ON. (b) Acts #1–#4 are turned ON. When the left end rises up transferring vertical contact force to the right (the cross-hatched region to impulse function $F_{g,1}$), torque balance requires that some vertical force is transferred from the right to the left side of the robot (indicated schematically the green line).

"friction asymmetry" necessary for inchworm motion. Fig. 16 shows the mechanism of contact force and friction asymmetry. We assume friction is positively correlated with contact force. So, an increase in contact force leads to an increase in friction. We begin with voltages V_2, V_3, and V_4 applied, so the middle three actuators curl up [Fig. 16(a)]. Then V_1 is applied to the left actuator, lifting it off the ground [Fig. 16(b)]. Because this section is no longer on the ground, the integrated amount of the contact force of this section, which was uniformly distributed, now becomes a delta function $F_{g,1}$ at the point where the actuator lifts off the ground.

This rightward shift of contact force induces an imbalance in the torque between the left and right ends of the robot, which previously canceled each other out by symmetry. To maintain a torque balance consistent with the robot shape, an amount ΔF_{Ground} of the right contact force delta function is transferred to the left side, in a "seesaw balance" type of effect. This results in the desired "friction asymmetry" between the left and right ends of the robot, as required for "inchworm" motion.

We now calculate the magnitude of this ΔF_{Ground} [Fig. 16(b)]. Before raising the actuator, $F_{G,2B}$ and $F_{G,4B}$ each represent half of the mass of the suspended section

$$F_{g,2B} = F_{g,4B} = \frac{1}{2} qg L_{\text{SUS,MID}}. \tag{23}$$

where $L_{\text{SUS,MID}}$ is the suspended length of the middle three actuators (10).

When Actuator #1 is raised, the contact force of the suspended section is transferred to a delta function $F_{g,1}$ [Fig. 16(b)], where $F_{g,1} = qgL_{\text{SUS,LEFT}}$. We now compare the torque on the left and right sides of the middle of the robot about its center, to find ΔF_{Ground}. On the left side, the torque is

$$\begin{aligned}\tau_L = {} & F_{g,1}\left(\frac{5}{2}L - L_{\text{SUS,LEFT}}\right) \\ & - qgL_{\text{SUS,LEFT}}\left(\frac{5}{2}L - \frac{1}{2}L_{\text{SUS,LEFT}}\right) \\ & + F_{g,2C}\frac{1}{2}L_{\text{SUS, MID}}.\end{aligned} \tag{24}$$

$F_{g,2C}$ is the discrete contact force at the left side of the midsection [Fig. 16(b)]. The right side torque is

$$\tau_R = F_{g,4C}\frac{1}{2}L_{\text{SUS, MID}} \tag{25}$$

where $F_{g,4C}$ is the impulse contact force at the right side of the midsection [Fig. 16(b)]. Equating these two torques gives

$$\begin{aligned} & F_{g,1}\left(\frac{5}{2}L - L_{\text{SUS,LEFT}}\right) + F_{g,2C}\frac{1}{2}L_{\text{SUS,MID}} \\ & = F_{g,4C}\frac{1}{2}L_{\text{SUS,MID}} + qgL_{\text{SUS, LEFT}}\left(\frac{5}{2}L - \frac{1}{2}L_{\text{SUS,LEFT}}\right)\end{aligned} \tag{26}$$

and

$$F_{g,2C} + F_{g,4C} = qgL_{\text{SUS,MID}}. \tag{27}$$

Therefore,

$$F_{g,2C} = \frac{1}{2}qgL_{\text{SUS,MID}} + \frac{qgL^2_{\text{SUS,LEFT}}}{2L_{\text{SUS,MID}}} \tag{28}$$

$$F_{g,4C} = \frac{1}{2}qgL_{\text{SUS,MID}} - \frac{qgL^2_{\text{SUS,LEFT}}}{2L_{\text{SUS,MID}}} \tag{29}$$

$$\begin{aligned}\Delta F_{\text{Ground}} & := F_{g,4B} - F_{g,4C} \\ & = \frac{qgL^2_{\text{SUS,LEFT}}}{2L_{\text{SUS,MID}}}.\end{aligned} \tag{30}$$

The difference in the total vertical contact force between the two sides, which we call the force asymmetry F_{Asymm}, is then

$$\begin{aligned}F_{\text{Asymm}} & = 2\Delta F_{\text{Ground}} \\ & = \frac{qgL^2_{\text{SUS,LEFT}}}{L_{\text{SUS,MID}}}.\end{aligned} \tag{31}$$

As expected, the asymmetry in contact force increases as the suspended length of Actuator #1, $L_{\text{SUS,LEFT}}$, increases.

Thus, by raising one end of the robot, the total contact force on that end goes up, whereas going down on the other end, i.e., by lifting up one end of the robot, we increase its friction to the ground compared with the other end, effectively causing it to stick relative to the other end, as required for inchworm motion.

Of interest is the fractional effect—for example, the ratio of the difference in the left and right contact force versus the total

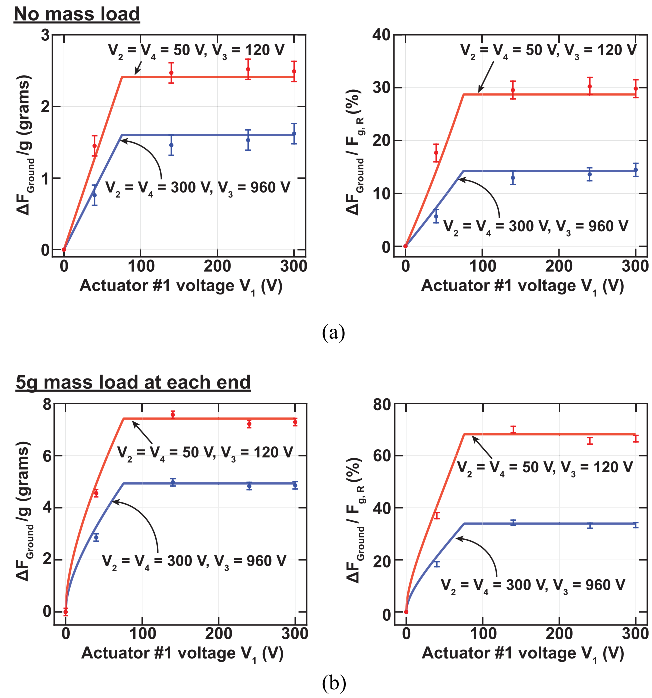

Fig. 17. Contact force asymmetry (F_{Asymm}) and the difference ratio ($F_{\mathrm{Asymm}}/F_{\mathrm{g,R}}$) as a function of the voltage of the lifting end (actuator #1), for (a) no mass loads at the end; (b) 5 g mass load at each end. The experiment is run in two different sets of voltages: (i) $V_2 = 300$ V, $V_{3,\text{exper't.}} = +1000$ V as shown in figure ($V_{3,\text{model}} = -580$ V), $V_4 = 300$ V, $V_5 = 0$ V; and (ii) $V_2 = 50$ V, $V_{3,\text{exper't.}} = +120$ V as shown in figure ($V_{3,\text{model}} = -70$ V), $V_4 = 50$ V, $V_5 = 0$ V. Error bars represent standard deviations.

contact force on the right half of the robot ($F_{g,R}$)

$$\frac{F_{\mathrm{Asymm}}}{F_{g,R}} = \frac{2L^2_{\mathrm{SUS,LEFT}}}{L^2_{\mathrm{SUS,MID}} + 2LL_{\mathrm{SUS,\,MID}} - L^2_{\mathrm{SUS,LEFT}}}. \tag{32}$$

From (32), $L_{\mathrm{SUS,MID}} = 30$ cm and $L_{\mathrm{SUS,LEFT}} = 10$ cm as an example, $F_{\mathrm{Asymm}}/F_{g,R} = 14\%$, implying the friction on the left side is 14% more than on the right side.

The relationship between the ratio and the actuator voltages can be calculated by substituting $L_{\mathrm{SUS,\,LEFT}}$ and $L_{\mathrm{SUS,\,MID}}$ from (2) and (10), when $L_{\mathrm{SUS,\,LEFT}} \leqslant L$ and $L_{\mathrm{SUS,\,MID}} \leqslant 3L$

$$\frac{F_{\mathrm{Asymm}}}{F_{g,R}} = \frac{2\gamma V_1}{\left(\sqrt[3]{18\left(\frac{qg}{EI}\right)\left[\gamma L(V_2 + V_3)\right]^2} + \sqrt{2\frac{qg}{EI}\gamma V_1}L - \gamma V_1\right)}. \tag{33}$$

2) Experiments: Experiments were conducted to validate the contact force difference between the two ends. Five scales (each 9 cm long) were put in a row under the robot, one per actuator, to measure the total contact force of each section of the robot.

Fig. 17(a) plots the force asymmetry F_{Asymm} and the ratio $F_{\mathrm{Asymm}}/F_{g,R}$, from model and experiment as a function of the applied voltages, in two cases: i) $V_2 = 300$ V, $V_3 = -580$ V in modeling (+1000 V in experiment with Type P1 actuator), $V_4 = 300$ V, and $V_5 = 0$ V; and ii) $V_2 = 50$ V, $V_3 = -70$ V (+120 V in experiment with Type P1 actuator), $V_4 = 50$ V, and $V_5 = 0$ V. Error bars represent standard deviations. Model and experiments match well. For our parameters with real-world actuators, the ground contact force is as much as 30% higher on the left end than on the right end.

3) Discrete Masses to Increase Friction Asymmetry: Given that surface friction can be highly nonuniform and/or nonlinear, due to varying surface roughness and other effects, a difference in contact force of 30% could prove too small to robustly fix one end of the inchworm robot versus the other. We now show this asymmetry can be increased by appropriately placed discrete mass loads. Consider discrete loads m_{load} placed on both ends of the robot. With the extra mass, the suspended length of Actuator #1 goes down, but fractionally by a smaller amount than the mass of the suspended length. This leads to a larger ground-force difference between the two sides

$$F_{\mathrm{Asymm}} = \frac{qgL^2_{\mathrm{SUS,LEFT}} + 2m_{\mathrm{load}}gL_{\mathrm{SUS,LEFT}}}{L_{\mathrm{SUS,MID}}} \tag{34}$$

and

$$\begin{aligned}\frac{F_{\mathrm{Asymm}}}{F_{g,R}} = &\left[2L^2_{\mathrm{SUS,LEFT}} + \frac{4m_{\mathrm{load}}gL_{\mathrm{SUS,LEFT}}}{qg}\right] \\ &/(L^2_{\mathrm{SUS,MID}} + 2LL_{\mathrm{SUS,MID}} + \frac{2m_{\mathrm{load}}L_{\mathrm{SUS,MID}}}{q} \\ &- L^2_{\mathrm{SUS,LEFT}} - \frac{2m_{\mathrm{load}}L_{\mathrm{SUS,LEFT}}}{q}).\end{aligned} \tag{35}$$

Fig. 17(b) shows data which repeats the experiment and model comparison of Fig. 17(a), but with a 5 g mass on both ends of the robot. It plots the ground force difference ratio for the same voltages with 5 g mass load at each end of the robot. The difference is boosted to 70% from an earlier value of 30%.

4) Experimental Validation of Adjustable "friction": We now demonstrate that lifting the left end of the robot (without the added-on discrete mass) increases its friction compared with the right end, when the total robot length is extended or contracted as in Fig. 1. For these experiments, the robot rests on a smooth plastic (acrylic) sheet.

First, as a control, Actuators #1 and #5 are not powered, and Actuators #2, #3, and #4 are cycled ON (voltages 300, 1000, and 300 V, respectively, in experiment) and OFF to laterally shrink and extend the robot [Fig. 18(a)]. Based on the height when the actuators #2, #3, and #4 are ON, the change in lateral length of the robot is estimated to be 1.2 mm (Section III-B6). With similar friction on either end (a symmetric condition), a change in the right end position of ~0.6 mm is observed over each half-cycle, half of the total length contraction (the left end was observed to symmetrically move by a similar amount in the other direction, data not shown).

The left end of the robot was then held in a raised position ($V_1 = 300$ V), and the cycling of the previous figure was repeated [Fig. 18(b)]. In this case: the left end of the robot is now fixed, moving much less than 0.1 mm, whereas the right end moves back and forth by the full 1.2 mm.

This comparison confirms that we can fix one end of the robot to the ground by lifting up the actuator on that end, as required for inchworm motion.

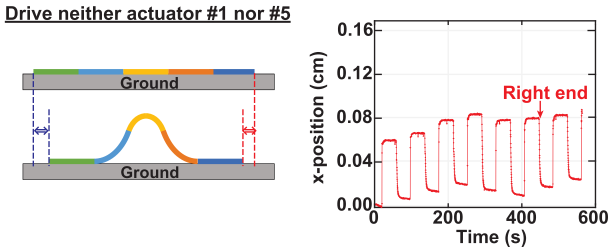

(a)

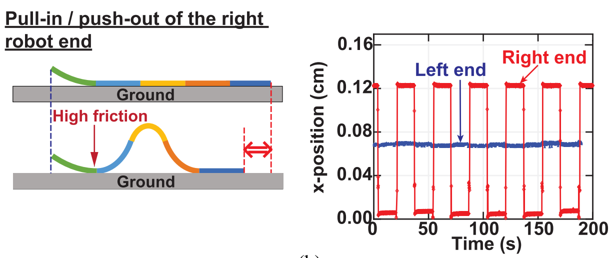

(b)

Fig. 18. Validation of motion mechanism for robot lateral motion, in two cases where Actuators #2, #3, and #4 are cyclically turned ON and OFF to laterally shrink and expand the central robot section by ∼12 mm. (a) Horizontal position of the right end of the robot versus time, when both Actuators #1 and #5 are left OFF(so they are flat on the ground), and the ends expand and contract symmetrically. (b) Actuator #1 is held in the air to increase friction at the Actuator #1–#2 interface, so that the left end is held fixed and all the lateral expansion and contraction occurs on the right end.

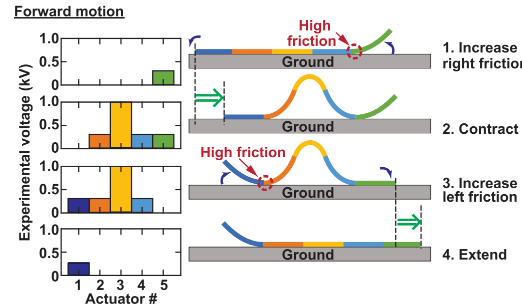

(a)

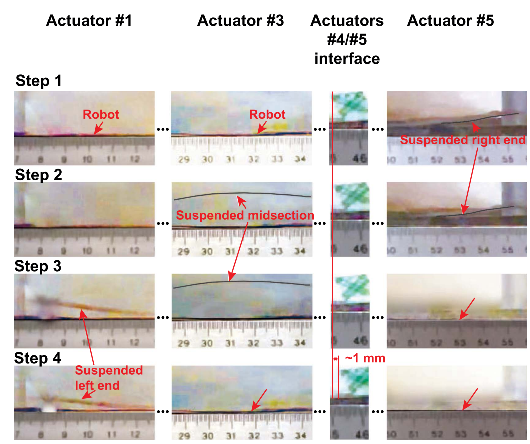

(b)

Step	Left end	Center	Right end
Step 1 Experiment Model	 0 mm 0 mm	 0 mm 0 mm	 0 mm 0 mm
Step 2 Experiment Model	 1.0 mm 1.2 mm	 0.5 mm 0.6 mm	 0 mm 0 mm
Step 3 Experiment Model	 0 mm 0 mm	 0 mm 0 mm	 0 mm 0 mm
Step 4 Experiment Model	 0 mm 0 mm	 0.5 mm 0.6 mm	 1.0 mm 1.2 mm

(c)

Fig. 19. (a) Robot motion design: one four-step cycle realizing forward motion. (b) Close-up images of the robot at four positions during each of the four steps of the motion cycle. At the interface between actuators 4 and 5, a lightweight “flag with an X” was taped to the robot to be able to discern the lateral motion. The x-scale of images at the interface between actuators 4 and 5 is magnified by 1.3X compared to that at other image locations. During step 4, the robot moves rightward ∼1 mm. (c) Experimental and model Lateral movement of left end, center, and right end in one cycle. The experimental error for all the movements is 0.2 mm.

V. Robot Inchworm Motion

This section experimentally demonstrates the motion of the inchworm robot. Results are compared with model predictions for forward motion, backward motion, and the effect of cycling frequency.

Fig. 19(a) shows the design of one cycle of its forward motion with four steps per cycle, and the voltages supplied for each step. For the forward motion:

i) V_1 is turned OFFso that the left end lays flat, and V_5 is turned ON to lift up the right end, increasing its friction to the ground compared with that on the left end;
ii) $V_2 - V_4$ are turned ON to make the middle three actuators curl up, so the left end moves rightward;
iii) V_5 is turned OFF to lower the right end and V_1 is turned ON to lift the left end, increasing friction on the left end;
iv) The middle section flattens as V_2–V_4 are turned OFF, so that the right end moves to the right; and
v) Return to Step 1 to complete a cycle, with the entire inchworm moving to the right.

The backward motion is similar to the forward motion, but the sequence of the steps is reversed.

Fig. 19(b) shows close-up experimental video images of the robot's shape and motion during one cycle. After each cycle, the robot moves rightward (forward) ∼1 mm. Fig. 19(c) compares the movement of this cycle with the model prediction for the robot's left end, center, and right end. It again shows a qualitative match between the experiment and the model.

Fig. 20(a) and (b) demonstrate forward and backward motion of the robot, with a time of 5 s per step. Both figures show the position of the left end of the robot. Forward motion averages 0.78 mm/cycle and reverse motion 0.66 mm/cycle. These figures demonstrate the ability to fix one end of the robot to the ground versus the other end (a requirement for “inchworm” motion), by raising the actuator on the end to be fixed, thereby increasing the friction on that end of the robot. Note, in the reverse motion

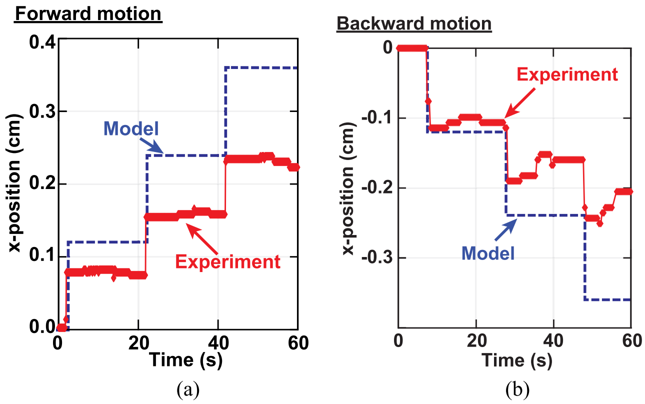

Fig. 20. Inchworm motion of the robot showing the lateral position of its left end (experiment vs. model prediction). (a) The forward motion of the robot using the cycle of Fig. 19(a). (b) Backward motion. When turned on, the applied voltages in the experiment were $V_1 = 300$ V, $V_2 = 300$ V, $V_3 = 1000$ V (equivalent to -580 V in modeling), $V_4 = 300$ V, and $V_5 = 300$ V. The robot moves 0.78 mm on average for each cycle of forward motion, and 0.66 mm/cycle for backward motion.

there is some evidence of the left end "backsliding" during the contraction cycle, accounting for the difference.

The model predicts $\sim$1.2 mm/cycle, whereas the experiment shows a result 30% smaller. The difference might come from the nonideal sliding of the "fixed" end for some cycles (since Fig. 18(b) shows 1.2 mm movement). Other sources of errors could include uncertainties in the experimental material parameters, such as epoxy thickness between the piezoelectric device and the substrate, nonideal stresses, or deformations in the as-assembled robot.

At low frequencies ($>$ 1 s periods), the lateral motion per cycle was independent of frequency, and a speed of 0.8 mm/s was achieved at 1 Hz [Fig. 21(a) and (b)]. When the frequency reaches $\sim$1 Hz, dynamic effects begin to become important, and at higher frequencies the motion slows down and surprisingly the robot can even go backward. [Fig. 21(b)] The motion here is no longer an inchworm-like motion. Given that a single actuator (suspended on one end) has a resonance frequency of $\sim$23 Hz (Fig. 24), and that multiple suspended actuators, as in the central section of the robot, will have a much lower resonant frequency, the observed transition of robot motion/cycle at $\sim$1 Hz between the quasistatic inchworm-motion regime and a more complicated dynamic motion is reasonable. Modeling of motion in the high-frequency regime is a subject of current investigation.

The energy consumption of the motion is calculated with capacitor charging/discharging models for the actuators, as piezoelectric is an insulator with little static current. For the inchworm motion, all the actuators charge and discharge only once per cycle. Therefore, the energy consumption per movement cycle is

$$\varepsilon = \sum_{i=1}^{5} C_i V_i^2. \tag{36}$$

By substituting the capacitance (C_i) of the actuators [29] and our operational voltages (V_i), the consumed energy per cycle is $\varepsilon = 17$ mJ.

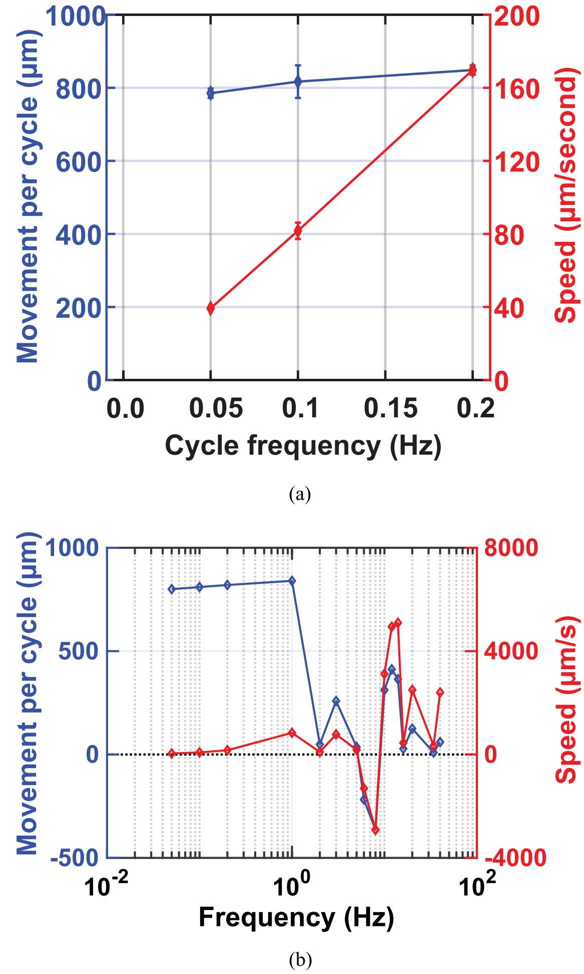

Fig. 21. (a) Robot inchworm movement per cycle and speed versus driving frequency: As the driving cycle period duration changes from 20 s (0.05 Hz) to 5 s (0.2 Hz). The movement per cycle is approximately constant so the average speed increases linearly with driving frequency. (b) Robot movement per cycle and speed versus driving frequency up to 40 Hz (frequency axis is in a logarithmic scale) [20].

VI. Model Implications, Scaling, and Limits

A. Length and Thickness Scaling

In this section, with a goal of making a smaller robot, we briefly examine how inchworm movement per cycle (L_x) scales with the size of the robot, assuming the length of all elements scales as S_L and the thicknesses of all layers scale by a factor S_t, where $S_t < 1$ for shrinking. (Ignoring aerodynamic effects, as in the rest of the article, robot width W has no effect.) We assume that the piezoelectric effects are large compared with gravity, as they are in the data presented earlier, so (17), which is the motion traveled per cycle, becomes

$$L_{x,\text{contract}} = \frac{1}{18}\left(V_3 + V_4\right)^2 \gamma^2 L^3. \tag{37}$$

Assuming Type P1 actuators, which depend on the lateral electric field in the piezoelectric layer due to the d_{33} coefficient and have many interdigitated fingers, changing the length changes the number of fingers, but does not change the maximum lateral electric field or maximum voltage in each section. Thus, α

(free-standing piezoelectric expansion per volt) is independent of S_L and S_t. Because E_1 (Young's modulus of the piezoelectric) also does not depend on voltage or thickness, and the second moment of area per unit width I scales as ${S_t}^3$, the curvature per voltage (38) $\gamma = \alpha(z_1 E_1 h_1/EI)$ scales as $1/S_t$.

Thus, the distance traveled per cycle $L_{x,\text{contract}}$ scales as S_L^3/S_t^2. Thus, if the thicknesses are scaled as 3/2 power of the lengths, the robot's motion per cycle is independent of changing its length. (Assuming Type P2 actuators lead to the same result.)

For example, for a length scaling factor S_L of 0.1 (meaning shrinking from the experimental 500 to 50 mm) and a thickness scaling factor of S_t of $(0.1)^{1.5} = 0.03$, with the same piezoelectric electric field, the robot's speed would be unchanged at $\sim$1 mm/s.

B. Routes Toward Higher Speed

Other inchworm robots have shown speeds up to 5 mm/s using mechanisms of pneumatic-driven fixing [41] and embedded magnets [14], respectively. We briefly mention several routes toward higher speed for piezoelectric robots of our general design. First, stronger piezoelectrics (more bending) would increase the motion per cycle. While our commercial piezoelectrics have a d_{33} of 460 pC/N, in more advanced piezoelectric d_{33} can reach 2400 pC/N [42], 2820 pC/N [43], and even 6300 pC/N [44], over 10$\times$ larger than those of the actuators used in our work. In principle, this would lead to a 10$\times$ increase in α (free-standing strain per volt) and, thus, a 10$\times$ increase in γ (curvature per volt), and thus, an increase in movement per cycle (37) by 10^2 to over 100 mm/s. An increase in the maximum electric field in the piezoelectric would have a similar effect.

Second, as shown in Fig. 21(b), dynamic effects, which give an observed shape very different than that of the "classic inchworm," can lead to higher speeds (e.g., 5 mm/s at 14 Hz). A full understanding of such dynamic effects and how they might be exploited is an area of ongoing work. Finally, we note that a similar robot in our lab driven at 14 Hz actually jumps completely off the ground (with a cyclical motion at 7 Hz!) [20]. How to understand and exploit such a phenomenon for faster motion will require a thorough understanding of nonlinear dynamic effects and damping in the robot, well beyond the scope of this article.

C. Surface Variability or Incline

In Section IV-B, we analyzed how much contact force difference between the two ends we can generate by changing the robot's shape. Without an extra payload, the difference reaches 14% and with an extra 5 g on both ends, it reaches 70%. These numbers describe how much difference in friction coefficient between the two ends (due to a spatially-varying surface roughness, for example) the robot can tolerate for ideal inchworm motion. If the surface is inclined, the robot must not side downhill. Assuming uniform friction and angle of slope θ_{slope}, the "no slide" condition requires $\theta_{\text{slope}} < \arctan\mu$ where μ is the friction coefficient. Assuming $\mu = 0.7$, this corresponds to a slope of 35°.

VII. Conclusion

Previous work incorporating piezoelectrics into robots has generally relied only on a single actuator for each actuation element. These include a jumping cockroach robot with a single actuator [5], a robotic bee with flapping wings [6], and a robotic fish with a single actuator as its bending tail [45].

In this work, we introduced a new mechanism for robot motion, which inherently depends on the coordinated motion of multiple (five) piezoelectric actuators, by adjusting the friction of one end versus that on the other end of a multielement linear piezoelectric inchworm—namely, a "seesaw" effect. When one end is lifted off the ground, torque balance results in a higher "contact force" and, thus, friction to the ground on that end of the robot. Cycling this effect from one end to the other increases the friction of one end versus the other. No extra physical features such as adhesive or high-friction coating were required. Coupled with a cyclic contraction and expansion of the central section due to the central actuators, the inchworm moved forward or backward as desired.

Second, to guide our experiments, we developed a first-principle analytical soft-body model for the shape of a linear piezoelectric actuator array with different voltages on different actuators. Key novel aspects are the inclusion of the effect of gravity on the shape, and how the "contact force" is transferred when sections of the robot lift off the ground. This last effect leads to an asymmetry between the two ends, required for inchworm-type motion.

The models yield excellent matches to experiments on three different levels, all without any adjustable parameters. First, the shape of actuators is well predicted in the presence of gravity, including prediction of how much of the robot lifts off the ground for given applied voltages. Second, as one end of the robot lifts off the ground, how the contact force of the robot on the ground moves from one end to the other is well predicted. This was critical for the ultimate lateral motion of the inchworm. Third, motion in both forward and backward directions of 0.1 cm/cycle was predicted.

The robot should be well suited for exploring environments with a small vertical clearance ($\sim$1–2 cm). While the mechanics of swimming would be different than those discussed here, a similar multielement thin-film piezoelectric robot 100% suspended in air [46] was seen to "swim" forward near a surface when a traveling wave was applied. With suitable electrical insulation, the robot of this article, with much stronger piezoelectrics than the polymer piezoelectrics in [46], might be adapted for swimming in water.

Ongoing work includes faster cycling times for increased speed, modeling system dynamics, and integration of batteries, high-voltage electronics, and a bluetooth microcontroller directly onto the robot for tetherless operation [3], [39], [40].

Appendix A

A. Notations and Definitions

1) Input Material Parameters: The material parameters used in the model (Table I) are taken from the datasheet of the actuator

TABLE I
INPUT MATERIAL PARAMETERS

Symbol	Description	Value	Measured (M) / Specified (S)
E_1	Young's modulus of the PZT device	30 GPa	S
E_2	Young's modulus of the bonding epoxy	1.5 GPa	S
E_3	Young's modulus of the substrate	203 GPa	S
ρ_1	PZT device density	3.2 g/cm^3	S
ρ_2	Epoxy density	1.1 g/cm^3	S
ρ_3	Steel substrate density	7.9 g/cm^3	S
h_1	Thickness of the PZT device	300 μm	S
h_2	Thickness of the bonding epoxy	93 μm	M
h_3	Thickness of the substrate	50.8 μm	S
L	Length of a single actuator	10 cm	S
α	Free standing strain per Volt	1.3 ppm/V for type P1 actuators and 0.75 ppm/V for type P2 actuators	S

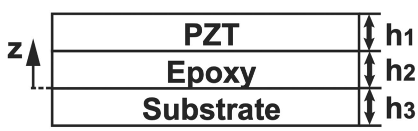

Fig. 22. Cross-sectional sketch of the trimorph structure: Piezoelectric layer PZT on the top, bonding epoxy in between and then substrate with thickness h_1, h_2, and h_3.

manufacturer, except for the bonding epoxy thickness h_2, which is measured experimentally.

2) Other Notations of the Model: Other notations of the model are shown in Nomenclature.

B. Bending Mechanism of the Actuator

A single actuator consists of three layers: The top layer is a PZT device, the middle layer is bonding epoxy, and the bottom layer is a steel substrate. This section describes the bending mechanism of such an actuator and its design optimization.

Fig. 22 shows the cross-sectional view of the trilayer structure of an actuator, with PZT thickness h_1, bonding epoxy thickness h_2, and substrate thickness h_3. When voltage is applied, the PZT tends to extend, but the substrate tends not to. The result is that the whole structure bends concave down. The bending curvature is, referenced w.r.t. the neutral axis [38]

$$\kappa = \frac{1}{R} = \alpha V \frac{z_1 E_1 h_1}{EI} = \gamma V \tag{38}$$

where α is the free-standing strain per Volt of the first layer. $z_i (i = 1, 2, 3)$ is the position of the central axis for each layer w.r.t. the neutral axis, E_i is Young's modulus for ith layer, EI

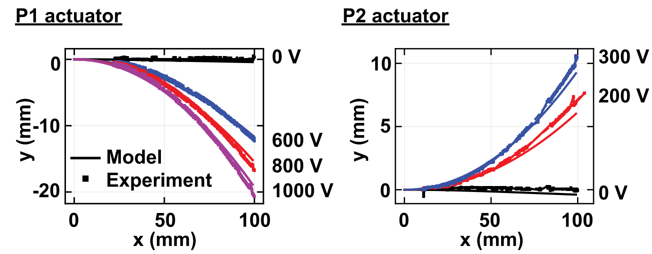

Fig. 23. Height versus distance for experimental piezoelectric actuators clamped horizontally on their left end. Characterization and modeling of experimental piezoelectric actuators validation for single actuator cantilever settings. A single actuator is floated in the air, the top surface facing up, clamped on its left end. Both Type P1 actuators (a type of actuator that prefers to bend down) and Type P2 actuators (prefer to bend up) are tested.

is the flexural rigidity per unit width of the whole structure, α is the free-standing voltage expansion coefficient, V is the applied voltage, and γ is the bending curvature per unit voltage. We would have

$$EI = \sum_{i=1}^{3} E_i (I_i + h_i z_i^2) \tag{39}$$

where

$$I_i = \frac{1}{12} h_i^3 \tag{40}$$

and the position of the neutral axis is

$$z_N = \frac{\sum_i z_i E_i h_i}{\sum_i E_i h_i}. \tag{41}$$

C. Characterization and Modeling of Experimental Piezoelectric Actuators

Fig. 23 shows model validation in single actuator cantilever settings. A single actuator, as described in Section II, is floated in the air with its left end clamped. Two kinds of actuators we used on the robot are tested here: One prefers to bend down (called "Type P1 actuator"), and the other prefers to bend up (called "Type P2 actuator"). In both scenarios, gravity takes into effect to pull the actuator down. The voltage ranges that they can take are also different. Vision sensing described in Section III-B4 is used to extract the shape of the actuators for different applied voltages. Each actuator is 10 cm long. A Type P1 actuator can bend down by about 2 cm with 1000 V supplied from a 5 V-to-1000 V power converter, and a Type P2 actuator can bend up by about 1 cm with 300 V applied. The experimental results all have good agreements with the modeling results.

Fig. 24 shows the dynamic behaviors of an actuator in a cantilever setting, with an applied sinusoidal voltage between 0 V and 1000 V. The resonant frequency is 23 Hz. Note that the operational bandwidth of the piezoelectric device is up to 10 kHz [29].

D. Actuator Performance Optimization

Actuator's bending performance is optimized by tuning the thickness of the substrate. If the substrate is too thin, it is very

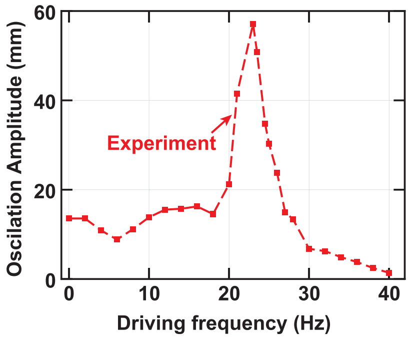

Fig. 24. Dynamics single-actuator cantilever showing achieved oscillation amplitude versus frequency with applied sinusoidal voltages.

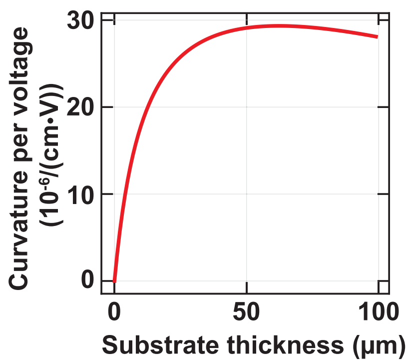

Fig. 25. Actuator bending performance optimization: Bending curvature as a function of substrate thicknesses.

soft so that it would not bend but extends together with the piezoelectric device. If the substrate is too thick, it is too stiff to be bent by piezoelectricity. Therefore, there is a sweet spot of substrate thickness that optimizes the performance. This trade-off needs to be taken into consideration when designing the actuators.

Fig. 25 shows the bending curvature as a function of substrate thickness. The thickness of the bonding epoxy is measured experimentally, and all other material parameters are taken from commercially available products. The bending curvature reaches its maximum when the substrate thickness is 65 μm. Therefore, the substrate thickness is picked to be 50 μm, the nearest one to the optimal point commonly available.

Acknowledgment

The authors would like to thank Prof. M. Haataja of Princeton University for his advice on mechanical modeling.

References

[1] M. T. Tolley et al., "A resilient, untethered soft robot," *Soft Robot.*, vol. 1, no. 3, pp. 213–223, Sep. 2014. [Online]. Available: https://www.liebertpub.com/doi/10.1089/soro.2014.0008

[2] T. Duggan, L. Horowitz, A. Ulug, E. Baker, and K. Petersen, "Inchworm-inspired locomotion in untethered soft robots," in *Proc. IEEE 2nd Int. Conf. Soft Robot.*, 2019. pp. 200–205.

[3] H. Cheng, Z. Zheng, P. Kumar, Y. Chen, and M. Chen, "Hybrid-SoRo: Hybrid switched capacitor power management architecture for multi-channel piezoelectric soft robot," in *Proc. IEEE Appl. Power Electron. Conf. Expo.*, 2022, pp. 1338–1344.

[4] X. Ji et al., "An autonomous untethered fast soft robotic insect driven by low-voltage dielectric elastomer actuators," *Sci. Robot.*, vol. 4, no. 37, Dec. 2019, Art. no. eaaz6451. [Online]. Available: https://robotics.sciencemag.org/lookup/doi/10.1126/scirobotics.aaz6451

[5] Y. Wu et al., "Insect-scale fast moving and ultrarobust soft robot," *Sci. Robot.*, vol. 4, no. 32, Jul. 2019, Art. no. eaax1594. [Online]. Available: https://robotics.sciencemag.org/lookup/doi/10.1126/scirobotics.aax1594

[6] N. T. Jafferis, E. F. Helbling, M. Karpelson, and R. J. Wood, "Untethered flight of an insect-sized flapping-wing microscale aerial vehicle," *Nature*, vol. 570, no. 7762, pp. 491–495, Jun. 2019. [Online]. Available: https://www.nature.com/articles/s41586-019-1322-0

[7] A. Dashtpour, "The cutest worm I have ever seen in my life," *Instagram*. Accessed: Feb. 6, 2024. [Online]. Available: https://www.instagram.com/p/COvZDT_qwac/

[8] B. Mosadegh et al., "Pneumatic networks for soft robotics that actuate rapidly," *Adv. Funct. Mater.*, vol. 24, no. 15, pp. 2163–2170, Apr. 2014. [Online]. Available: https://onlinelibrary.wiley.com/doi/10.1002/adfm.201303288

[9] R. Das, S. P. M. Babu, F. Visentin, S. Palagi, and B. Mazzolai, "An earthworm-like modular soft robot for locomotion in multi-terrain environments," *Sci. Rep.*, vol. 13, no. 1, pp. 1–14, 2023, doi: 10.1038/s41598-023-28873-w.

[10] L. Xu et al., "Locomotion of an untethered, worm-inspired soft robot driven by a shape-memory alloy skeleton," *Sci. Rep.*, vol. 12, no. 1, pp. 1–16, 2022.

[11] T. Du, L. Sun, and J. Wan, "A worm-like crawling soft robot with pneumatic actuators based on selective laser sintering of TPU powder," *Biomimetics*, vol. 7, no. 4, 2022, Art. no. 205.

[12] E. B. Joyee and Y. Pan, "A fully three-dimensional printed inchworm-inspired soft robot with magnetic actuation," *Soft Robot.*, vol. 6, no. 3, pp. 333–345, 2019.

[13] S. Ijaz et al., "Magnetically actuated miniature walking soft robot based on chained magnetic microparticles-embedded elastomer," *Sensors Actuators, A: Phys.*, vol. 301, 2020, Art. no. 111707, doi: 10.1016/j.sna.2019.111707.

[14] K. Maeda, H. Shinoda, and F. Tsumori, "Miniaturization of worm-type soft robot actuated by magnetic field," *Jpn. J. Appl. Phys.*, vol. 59, no. SI, 2020, Art. no. SIIL04.

[15] H. Niu et al., "MagWorm: A. biomimetic magnet embedded worm-like soft robot," *Soft Robot.*, vol. 8, no. 5, pp. 507–518, Oct. 2021. [Online]. Available: https://www.liebertpub.com/doi/10.1089/soro.2019.0167

[16] C. Ahn, X. Liang, and S. Cai, "Bioinspired design of light-powered crawling, squeezing, and jumping untethered soft robot," *Adv. Mater. Technol.*, vol. 4, no. 7, pp. 1–9, 2019.

[17] M. Calisti, G. Picardi, and C. Laschi, "Fundamentals of soft robot locomotion," *J. Roy. Soc. Interface*, vol. 14, no. 130, May 2017, Art. no. 20170101. [Online]. Available: https://royalsocietypublishing.org/doi/10.1098/rsif.2017.0101

[18] H. H. Hariri, G. S. Soh, S. Foong, and K. Wood, "Locomotion study of a standing wave driven piezoelectric miniature robot for bi-directional motion," *IEEE Trans. Robot.*, vol. 33, no. 3, pp. 742–747, Jun. 2017. [Online]. Available: https://ieeexplore.ieee.org/document/7855815/

[19] R. Xie, M. Su, Y. Zhang, M. Li, H. Zhu, and Y. Guan, "PISRob: A. pneumatic soft robot for locomoting like an inchworm," in *Proc. IEEE Int. Conf, Robot, Autom.*, 2018, pp. 3448–3453.

[20] Z. Zheng et al., "Scalable simulation and demonstration of jumping piezoelectric 2-D soft robots," in *Proc. Int. Conf. Robot. Autom.*, 2022, pp. 5199–5204.

[21] J.-S. Koh and K.-J. Cho, "Omega-shaped inchworm-inspired crawling robot with large-index-and-pitch (LIP) SMA spring actuators," *IEEE/ASME Trans. Mechatron.*, vol. 18, no. 2, pp. 419–429, Apr. 2013.

[22] Y. Wu et al., "PRE-curved PVDF/PI unimorph structures for biomimic soft crawling actuators," in *Proc. IEEE Micro Electro Mech. Syst.*, 2018, pp. 581–584.

[23] J. Guo, C. Xiang, A. Conn, and J. Rossiter, "All-soft skin-like structures for robotic locomotion and transportation," *Soft Robot.*, vol. 7, no. 3, pp. 309–320, Jun. 2020. [Online]. Available: https://www.liebertpub.com/doi/10.1089/soro.2019.0059

[24] J. Huang et al., "Electrically programmable adhesive hydrogels for climbing robots," *Sci. Robot.*, vol. 6, no. 53, Apr. 2021, Art. no. eabe1858. [Online]. Available: https://robotics.sciencemag.org/lookup/doi/10.1126/scirobotics.abe1858

[25] M. P. Murphy and M. Sitti, "Waalbot: An agile small-scale wall-climbing robot utilizing dry elastomer adhesives," *IEEE/ASME Trans. Mechatron.*, vol. 12, no. 3, pp. 330–338, Jun. 2007. [Online]. Available: https://ieeexplore.ieee.org/document/4244394/

[26] M. Duduta, D. R. Clarke, and R. J. Wood, "A high speed soft robot based on dielectric elastomer actuators," in *Proc. IEEE Int. Conf. Robot. Autom.*, 2017, pp. 4346–4351.
[27] H. Guo, J. Zhang, T. Wang, Y. Li, J. Hong, and Y. Li, "Design and control of an inchworm-inspired soft robot with omega-arching locomotion," in *Proc. IEEE Int. Conf. Robot. Autom.*, 2017, pp. 4154–4159.
[28] W. K. Wilkie, "NASA MFC piezocomposites: A development history," in *Proc. Int. Symp. Macro Fiber Composite Appl.*, 2005, vol. 2014, pp. 27–28.
[29] Smart Material Corp., "MFC engineering properties (part numbers: M-8514-P1, M-8514-P2)," *smart-material.com*. Accessed: Feb. 6, 2024. [Online]. Available: https://www.smart-material.com/MFC-product-propertiesV2.html
[30] R. J. Webster and B. A. Jones, "Design and kinematic modeling of constant curvature continuum robots: A review," *Int. J. Robot. Res.*, vol. 29, no. 13, pp. 1661–1683, Nov. 2010. [Online]. Available: http://journals.sagepub.com/doi/10.1177/0278364910368147
[31] V. Falkenhahn, A. Hildebrandt, R. Neumann, and O. Sawodny, "Model-based feedforward position control of constant curvature continuum robots using feedback linearization," in *Proc. IEEE Int. Conf. Robot. Autom.*, 2015, pp. 762–767.
[32] C. D. Santina, A. Bicchi, and D. Rus, "On an improved state parametrization for soft robots with piecewise constant curvature and its use in model based control," *IEEE Robot. Autom. Lett.*, vol. 5, no. 2, pp. 1001–1008, Apr. 2020.
[33] N. Lobontiu, M. Goldfarb, and E. Garcia, "A piezoelectric-driven inchworm locomotion device," *Mechanism, Mach. Theory*, vol. 36, no. 4, pp. 425–443, Apr. 2001. [Online]. Available: https://linkinghub.elsevier.com/retrieve/pii/S0094114X00000562
[34] D. Bandopadhya, "Derivation of transfer function of an IPMC actuator based on pseudo-rigid body model," *J. Reinforced Plastics Composites*, vol. 29, no. 3, pp. 372–390, Feb. 2010. [Online]. Available: http://journals.sagepub.com/doi/10.1177/0731684408097778
[35] W.-B. Li, W.-M. Zhang, H.-X. Zou, Z.-K. Peng, and G. Meng, "A fast rolling soft robot driven by dielectric elastomer," *IEEE/ASME Trans. Mechatron.*, vol. 23, no. 4, pp. 1630–1640, Aug. 2018.
[36] B. A. Jones, R. L. Gray, and K. Turlapati, "Three dimensional statics for continuum robotics," in *Proc. IEEE/RSJ Int. Conf. Intell. Robots Syst.*, 2009, pp. 2659–2664.
[37] O. A. Bauchau and J. I. Craig, "Euler–Bernoulli beam theory," in *Structural Analysis. Solid Mechanics and Its Appl.*, vol 163. Berlin, Germany: Springer, 2009, pp. 173–221. [Online]. Available: http://link.springer.com/10.1007/978-90-481-2516-6_5
[38] M. Weinberg, "Working equations for piezoelectric actuators and sensors," *J. Microelectromech. Syst.*, vol. 8, no. 4, pp. 529–533, 1999.
[39] Z. Zheng et al., "Wirelessly-controlled untethered piezoelectric planar soft robot capable of bidirectional crawling and rotation," in *Proc. IEEE Int. Conf. Robot. Autom.*, 2023, pp. 641–647.
[40] H. Cheng et al., "eViper: A. scalable platform for untethered modular soft robots," in *Proc. IEEE/RSJ Int. Conf. Intell. Robot. Syst.*, 2023, pp. 604–611, doi: 10.1109/IROS55552.2023.10342402.
[41] X. Liu, M. Song, Y. Fang, Y. Zhao, and C. Cao, "Worm-inspired soft robots enable adaptable pipeline and tunnel inspection," *Adv. Intell. Syst.*, vol. 4, no. 1, 2022, Art. no. 2100128.
[42] D. Tanaka, T. Tsukada, M. Furukawa, S. Wada, and Y. Kuroiwa, "Thermal reliability of Alkaline Niobate-based lead-free piezoelectric ceramics," *Jpn. J. Appl. Phys.*, vol. 48, no. 9, Sep. 2009, Art. no. 09KD08. [Online]. Available: https://iopscience.iop.org/article/10.1143/JJAP.48.09KD08
[43] H. Cao and H. Luo, "Elastic, piezoelectric and dielectric properties of PB(mg 1/3 NB 2/3) o 3 −38%pbtio 3 single crystal," *Ferroelectrics*, vol. 274, no. 1, pp. 309–315, 2002, doi: 10.1080/00150190213965.
[44] J. Zhong et al., "Flexible PET/EVA-based piezoelectret generator for energy harvesting in harsh environments," *Nano Energy*, vol. 37, no. 1, pp. 268–274, Jul. 2017. [Online]. Available: https://linkinghub.elsevier.com/retrieve/pii/S2211285517303063
[45] R. K. Katzschmann, A. D. Marchese, and D. Rus, "Hydraulic autonomous soft robotic fish for 3D swimming," in *Springer Tracts in Adv. Robot.*, vol. 109. Cham, Switzerland, Springer, 2016, pp. 405–420. [Online]. Available: http://link.springer.com/10.1007/978-3-319-23778-7_27
[46] N. T. Jafferis, H. A. Stone, and J. C. Sturm, "Traveling wave-induced aerodynamic propulsive forces using piezoelectrically deformed substrates," *Appl. Phys. Lett.*, vol. 99, no. 11, Sep. 2011, Art. no. 114102. [Online]. Available: http://aip.scitation.org/doi/10.1063/1.3637635

Zhiwu Zheng (Member, IEEE) received the B.S. degree in physics from Nanjing University, Nanjing, China, in 2016, and the Ph.D. degree in electrical and computer engineering from Princeton University, Princeton, NJ, USA, in 2023.

He is currently a Senior Machine Learning Research Scientist with Analog Devices, Inc., Wilmington, MA, USA. His current research interests include machine learning and statistical signal processing algorithms, architectures, circuits and devices for advanced sensing systems, and robotics.

Dr. Zheng was the recipient of an ICRA Best Poster Award, an IROS Best Paper Finalist, a RoboSoft Outstanding Poster Award, 2018-2023 Fellowships of the Program in Plasma Science and Technology (PPST) at Princeton University, 2014 Shi Shi-Yuan Scholarship and 2014 Infineon Scholarship, as well as 2013–2016 Fellowships of China National Innovational Undergraduates Program, Nanjing University 2013 Excellent Student, 2013 Scientific Innovation Scholarship, and 2013–2014, 2014–2015, 2015–2016 First-Place Talent Scholar Awards.

Prakhar Kumar received the B.E.(Hons) degree in electrical and electronics engineering from BITS Pilani, Pilani, India, in 2016.

He is interested in designing technology platforms that can enable machine learning algorithms to carry out inference and state estimation tasks effectively. His current research interest focuses on developing hybrid sensing systems by bringing together large area electronics (LAE) and CMOS VLSI technologies.

Yenan Chen (Member, IEEE) received the bachelor's and Ph.D. degrees in electrical engineering from the College of Electrical Engineering, Zhejiang University, Hangzhou, China, in 2010 and 2018, respectively, and the Honors degree in engineering from Chu Kochen College, Zhejiang University, in 2010.

From 2018 to 2021, he was a Postdoctoral Research Associate with the Department of Electrical Engineering, Princeton University, Princeton, NJ, USA. Since December 2021, he has been a Principal Investigator with the ZJU-Hangzhou Global Scientific and Technological Innovation Center, Zhejiang University, where he has been a ZJU100 Professor with the College of Electrical Engineering since July 2023. He holds seven issued Chinese patents. His research interests include power electronic topology, architecture, and control for data center, renewable energy, and transportation.

Dr. Chen was the recipient of two Prize Paper Awards of IEEE Transactions on Power Electronics in 2021 and 2022, the IEEE COMPEL Best Paper Award in 2020, the IEEE Applied Power Electronics Conference and Exposition Outstanding Presentation Award in 2019, and the First Place Award from the Innovation Forum of Princeton University in 2019.

Hsin Cheng (Student Member, IEEE) received the B.S. degree in engineering from the Department of Electrical Engineering, National Taiwan University, Taipei, Taiwan, in 2020 and Ph.D. degree in electrical and computer engineering from Princeton University, Princeton, NJ, USA.

His research interests include high-voltage-conversion-ratio modular power architecture, design and mechanism of electroactive soft robots, and their intersections.

Sigurd Wagner (Fellow, IEEE) received the Ph.D. degree in physical chemistry from the University of Vienna, Vienna, Austria, in 1968.

He was a post-doc with Ohio State University, Columbus, OH, USA. From 1970 to 1978, he was with Bell Labs, and from 1978 to 1980, he was the Founding Chief of the Photovoltaic Research Branch with the Solar Energy Research Institute (now NREL). He is currently the Professor Emeritus of electrical engineering and Senior Scholar with Princeton University, where he has been working since 1980. He has been an advocate of laboratory-based learning. In collaboration with colleagues and students, he has introduced fundamentally new materials, concepts, devices, and structures to thin-film electronics: The first heterojunction solar cell with a ternary compound semiconductor, CuInSe2, and a quaternary compound, Cu2CdSnS4, among others; the Fermi-level dependence of the density of recombination center in hydrogenated amorphous silicon; microfluidic fundamentals of forming device patterns by printing, and the design and fabrication of microfluidic devices; foundational experiments on flexible, rollable, elastically stretchable, and conformably shaped electronic surfaces, and their basic design rules and architecture. At present he is working with his colleagues James C. Sturm and Naveen Verma on the demonstration of complete large-area hybrid thin-film/CMOS-circuit systems for sensing applications. His research interests include developing concepts and applications of large-area electronics.

Dr. Wagner was the recipient of the 2009 Nevill Mott Prize, the 2014 ITC 10th Anniversary Prize, and the 2017 MRS David Turnbull Lectureship. A plaque in Princeton's Electrical Engineering undergraduate laboratory honors his engagement in lab education. He is a Fellow of the American Physical Society, and a corresponding Member of the Austrian Academy of Sciences. He was an Alexander von Humboldt Foundation Senior Fellow.

Minjie Chen (Senior Member, IEEE) received the the B.S. degree in electrical engineering from Tsinghua University, Beijing, China, in 2009, and the S.M., E.E., and Ph.D. degrees in electrical engineering and computer science from Massachusetts Institute of Technology, Cambridge, MA, USA, in 2012, 2014, and, 2015, respectively.

He is currently an Assistant Professor of electrical and computer engineering and with the Andlinger Center forEnergy and the Environment, Princeton University, Princeton, NJ, USA. His research interests include high-frequency power electronics, power architecture, power magnetics, advanced packaging, data-driven methods, design automation, and design methods of high-performance power electronics for emerging and important applications.

Dr. Chen is the recipient of the IEEE PELS Richard M. Bass Outstanding Young Power Electronics Engineer Award, the Princeton SEAS E. Lawrence Keyes, Jr./Emerson Electric Company Junior Faculty Award, the NSF CAREER Award, six IEEE Transactions on Power Electronics Prize Paper Awards, a COMPEL Best Paper Award, an ICRA Best Poster Award, an IROS Best Paper Finalist, three ECCE Best Demo Awards, a 3D-PEIM Rao R. Tummala Best Paper Award, an OCP Best Paper Award, a Siebel Research Award, a C3.ai Research Award, a First Place Award of Princeton Keller Center Innovation Forum, and the MIT EECS D. N. Chorafas Ph.D. Thesis Award. He was listed on the Princeton Engineering Commendation List for outstanding teaching multiple times. He is the Vice Chair of PELS TC10 Design Methodologies, and the TPC Member of a few flagship PELS conferences including APEC, ECCE, COMPEL, and ICDCM.

Naveen Verma (Senior Member, IEEE) received the B.A.Sc. degree in electrical and computer engineering from the University of British Columbia, Vancouver, Canada, in 2003, and the M.S. and Ph.D. degrees in electrical engineering from Massachusetts Institute of Technology, Cambridge, MA, USA, in 2005 and 2009 respectively.

Since 2009, he has been with Princeton University, where he is currently the Director of the Keller Center for Innovation in Engineering Education, Princeton, NJ, USA, and a Professor of electrical and computer engineering. His research focuses on advanced sensing systems, exploring how systems for learning, inference, and action planning can be enhanced by algorithms that exploit new sensing, and computing technologies. His research interests include research on large-area, flexible sensors, energy-efficient statistical-computing architectures and circuits, and machine-learning and statistical-signal-processing algorithms.

Dr. Verma is the recipient or corecipient of the 2006 DAC/ISSCC Student Design Contest Award, 2008 ISSCC Jack Kilby Paper Award, 2012 Alfred Rheinstein Junior Faculty Award, 2013 NSF CAREER Award, 2013 Intel Early Career Award, 2013 Walter C. Johnson Prize for Teaching Excellence, 2013 VLSI Symp. Best Student Paper Award, 2014 AFOSR Young Investigator Award, 2015 Princeton Engineering Council Excellence in Teaching Award, and 2015 IEEE Trans. CPMT Best Paper Award. He was a Distinguished Lecturer of the IEEE Solid-State Circuits Society, and is currently on the Technical Program Committees for ISSCC, VLSI Symp., DATE, and IEEE Signal-Processing Society (DISPS).

James C. Sturm (IEEE Life, Fellow) was born in Berkeley Heights, NJ, in 1957. He received the B.S.E. degree in electrical engineering and engineering physics from Princeton University, Princeton, NJ, in 1979, and the M.S.E.E. and Ph.D. degrees in electrical engineering, in 1981 and 1985, respectively, both from Stanford University, Stanford, CA, USA.

In 1979, he was with Intel Corporation, Santa Clara, CA, as a Microprocessor Design Engineer, and in 1981 he was a Visiting Engineer with Siemens, Munich, Germany. In 1986, he joined the faculty of Princeton University, Princeton, NJ, where he is currently the Stephen R. Forrest Professor of electrical and computer engineering and the Chair of the Department of Electrical and Computer Engineering. From 2003 to 2015, he was the Founding Director with the Princeton Institute for the Science and Technology of Materials (PRISM). From 1994 to 1995, he was a von Humboldt Fellow with the Institut fuer Halbleitertechnik, the University of Stuttgart, Stuttgart, Germany. His research interests include the fields of silicon-based heterojunctions, thin-film and flexible electronics, photovoltaics, the nano-bio interface, SOI, and 3-D integration.

Dr. Sturm was the recipient of more than ten awards for teaching excellence. He was a National Science Foundation Presidential Young Investigator. In 1996 and 1997, he was the Technical Program Chair and General Chair of the Device Research Conference, respectively. He was with the organizing committee of IEDM (1988–1992 and 1998–1999), having chaired both the solid-state device and detectors/sensors/displays committees. He was on the Boards of Directors of the Materials Research Society and the Device Research Conference, and was a co-Founder of Aegis Lightwave.